Development of an Optically Accessible High-Pressure Strand Burner and the Experimental Determination of the Burn Rate of High Temperature Thermally Degraded HTPB/AP/AL Solid Propellant Combustion

by

Matthew Austin Phillips

A thesis submitted to the Graduate Faculty of
Auburn University
in partial fulfillment of the
requirements for the Degree of
Master of Science

Auburn, Alabama
December 12, 2020

Keywords: solid, propellant, thermally, degraded, burn, rate

Approved by

Dr. David Scarborough, Chair, Associate Professor of Aerospace Engineering
Dr. Brian Thurow, Professor of Aerospace Engineering
Dr. Roy Hartfield, Professor of Aerospace Engineering

Abstract

This thesis presents initial findings from solid propellant experiments using thermally degraded hydroxyl-terminated polybutadiene, ammonium perchlorate, and aluminum powder propellants. Currently, a better understanding of the burning characteristics of solid propellants when aged or thermally damaged using a high temperature degradation technique is needed. Past research investigated the effects of thermal aging while other studies focused on low temperature degradation of propellants. However, these approaches to gaining a holistic understanding of the burning characteristic of solid propellants has fallen short of a complete understanding of the effects of thermal aging on the burn characteristics of propellants. This research focused on measuring the burn rate of solid propellants with short time exposure to high temperatures to simulate a propellant being near a fire for a short time. Propellant samples were mixed and cured in-house using classical techniques. The propellant samples were thermally degraded in a laboratory oven at 538 K for 5 minutes. The samples were burned in an optically accessible, high pressure strand burner facility. For the study, data was acquired using high speed imaging. The burning line in the images was found using a novel MATLAB edge detection technique and a manual edge detection technique in MATLAB. The general results offer evidence that thermally degraded propellant samples resulted in higher burn rates with inconsistent burning.

Acknowledgments

I want to thank my wife for supporting me through this whole process. You have helped me to push through this process and I can't thank you enough for all the hours you put in with me at the lab and office so that I could complete this thesis. You have been my rock and cheerleader and can't thank you enough for your support.

I want to thank my parents, Matt and Cheri Phillips, and my sister, Amanda Phillips, for supporting my decision and cheering me on through my time in college. With your guidance and support I have progressed to where I am today. So, thank you very much, you three will never know how much I have appreciated your support.

I want to thank my parent-in-laws, Chris and Shelley Holzworth for their support through this time period. Your guidance and support helped me all along the way to finish and I am so appreciative of your guidance.

I want to thank Mr. Andy Weldon for all the teaching sessions in the shop and the many lessons learned. I know that the lessons you taught me will help me to become a better engineer and I want to thank you for everything you have done for me through my college career.

I want to thank Dr. Triggs for the immense amounts of knowledge that you passed on to me through my college experience. My passion for rockets and cars was certainly fueled by you and all that you taught me. I will always be grateful of your input and I want to thank you for everything.

Finally, I want to thank Dr. Scarborough for taking me on as a graduate student. You have helped mentor me into the engineer that I have become, and your guidance has pushed me farther than I thought I could achieve. So, thank you very much for taking a chance on me.

Table of Contents

Development of an Optically Accessible High-Pressure Strand Burner and the Experimental Determination of the Burn Rate of High Temperature Thermally Degraded HTPB/AP/AL Solid Propellant Combustion 1

Abstract 2

Acknowledgments 3

Table of Contents 5

List of Tables 7

List of Illustrations 8

List of Abbreviations 10

Chapter 1. Introduction 12

Chapter 2. Background and Literature Review 14

Chapter 3. Solid Propellant Testing Facilities 17

High Pressure Strand Burner 17

Propellant Mixing, Casting, and Curing Facilities 27

Thermal Aging Facilities 28

Diagnostics and Control 29

Image Processing 31

Chapter 4. Experimental Description 35

Error Analysis 37

Chapter 5. Results and Discussion 42

Chapter 6. Conclusions 64

Chapter 7. Bibliography 66

List of Tables

Table 1: Propellant Chemistries with Curing Date and Method..... 36

Table 2: Average Burning Rates of Propellant Formulations and the Associated Uncertainty Values..... 41

Table 3: Initial Burn Rate Data..... 44

Table 4: Average Regression Rate of the Tested Propellants..... 46

Table 5: Average Burn Rates from Tested Propellants 61

List of Illustrations

Fig. 1: Cross Sectional View of the Strand Burner Pressure Vessel 18

Fig. 2: Ansys Analysis of the Strand Burner Body with the Minimum FOS Marked..... 19

Fig. 3: Window Retention Plate with Minimum FOS Flagged 20

Fig. 4: Bottom Block with Minimum FOS Flagged 21

Fig. 5: Burst Disk Retention Plate with Minimum FOS Flagged..... 22

Fig. 6: Top Flow Plate with Minimum FOS Flagged 23

Fig. 7: Full Strand Burner Rig P&ID..... 24

Fig. 8: Sample Holding Fixture 25

Fig. 9: Propellant Samples in Quartz Tubes 26

Fig. 10: Sample Setup with Ignition System 27

Fig. 11: Propellant Samples in the Degradation Oven..... 29

Fig. 12: Image of Burning Propellant from High-Speed Camera..... 31

Fig. 13: (Left) Original Cropped Image and (Right) Complement of the original cropped image..... 33

Fig. 14: (Left) Image Used for Selecting Burning Line Manually and (Right) Masked Image..... 33

Fig. 15: Propellant 6 Burning at Two Different Points in Time During a Single Experimental Run 37

Fig. 16: Example of Atmospheric Conditions Break Wire Data 43

Fig. 17: Comparison Plots of Manual Image Processing to the Automated Process..... 45

Fig. 18: Undegraded Samples vs. Degraded Samples 47

Fig. 19: Unburned Area of Propellant vs. Time for Propellants with Aluminum; a and b are Propellant 1, c and d are Propellant 2, and e and f are Propellant 3 51

Fig. 20: Unburned Area of Propellant vs. Time for Propellants without Aluminum; a and b are Propellant 4, c and d are Propellant 5, and e and f are Propellant 6 53

Fig. 21: Average Area of Unburned Propellants with Aluminum Versus Time with Data Limits for the Deviated Unburned Area Data from the Average..... 55

Fig. 22: Average Area of Unburned Propellants without Aluminum Versus Time with Data Limits for the Deviated Unburned Area Data from the Average..... 56

Fig. 23: Burning Rate vs. Time for Propellants with Aluminum..... 58

List of Abbreviations

a empirical constant

f reaction rate factor

$k_{clamped}$ clamped edge parameter

p pressure (Pa)

P pressure difference (psi)

n empirical constant

r short length (in)

r_1 burning rate (mm/s)

R long length (in)

S_{MAX} design stress (psi)

t thickness of window (in)

t_1 approximated artificial age (years)

t_T time material was kept at elevated temperature (years)

T_s storage temperature (degree C)

T_t elevated temperature (degree C)

ΔT_R change in temperature that results in a doubling of the reaction rate (K)

x ratio of lengths

Chapter 1. Introduction

Solid rocket motors are widely used in military and civilian applications and are characteristically the paramount component in some of history's greatest rocket propelled launches: the boosters on the Space Shuttle, the booster on the Space Launch System, and the Javelin missile system. The origins of solid propellant date back to ancient China and were developed in the United States circa 1960[1]. Although much of the current research and development efforts in modern rocketry focus on liquid propellant engines, large quantities of solid rocket propellant are stored in the weapon storage facilities of our nation's military services and bases. Some propellants have been stored for future use for over ten years; however, the effects of prolonged and lengthy storage on the burning characteristics of aged solid rocket propellant is still somewhat unknown.

Solid propellants are typically composite propellants consisting of a solid oxidizer, a solid fuel, and a liquid polymer binder which has cure into a solid. The oxidizers ordinarily used are a composition of ammonium perchlorate (AP), ammonium nitrate, or potassium perchlorate. The oxidizer is bound to a fuel which is normally aluminum, boron, HMX, or RDX. Aluminum and boron are metal powder fuels, and HMX and RDX are energetic or explosive based fuels. These solid components are bound together with a polymer like hydroxyl-terminated polybutadiene (HTPB) or polybutadiene acrylonitrile referred to as PBAN. Lastly, a common propellant formulation such as ammonium perchlorate, aluminum, and hydroxyl-terminated polybutadiene is standard and utilized across multiple referenced works[2–8].

Rockets are designed to function with a known propellant burn rate. Changes in the burn rate due to any cause can lead to unpredictable rocket performance including outright failure. What is

needed is a better understanding of the effect of exposure to extreme high temperature on burn rate. This includes not only average burn rate, but any fluctuations in burn rate that might be induced by any potential propellant degradation. The premise of this study is that high temperature, short duration thermally degraded propellants exhibit a difference in the burning rate characteristics when compared to non-degraded propellants.

Chapter 2. Background and Literature Review

Solid rocket propellants are commonly used in the US military's missiles, rockets, and other weaponry. A few examples of weapon systems which utilize solid rocket motors (SRM's) are the Hellfire missile[6], the Trident rocket[7], and the RUR-5 ASROC torpedo[9]. A commonly used composite propellant chemistry is hydroxyl-terminated polybutadiene (HTPB) as the binder, ammonium perchlorate (AP) as the oxidizer, and aluminum powder (AL) as the fuel. Past research has investigated the different characteristics of HTPB/AP propellant mixtures, yet there is still much to learn.[3]

The use of SRM's with unknown characteristics in adverse conditions could lead to catastrophic effects. Therefore, accurate knowledge of the burn rate and other propellant burning characteristics are important in order to design SRM's. The burn rate of a propellant can be affected by the thermal environment and how long it has been stored in that environment. The aging of a solid propellant can be simulated by thermal degradation which can be quantified and modeled by the Arrhenius equation as seen in the study by Thomas[4]. A study by Kadiresh et al. determined that the burn rate of thermally degraded propellant samples is minimally affected at low pressures and increases with higher pressures[3]. The majority of studies on the effects of thermally degraded solid propellants focus on the material properties such as fracture behavior and other viscoelastic measurements[2,8]. Ide et al not only tested propellant samples exposed to 60°C ambient temperature, but also samples exposed to -40°C[2]. The range of time the propellant samples were subjected to altered environments differed across past studies. However, propellants subjected to high temperatures for short periods of time lack prior research.

Examining exposure to high temperatures for short periods of time simulates a fire occurring near a weapons storage facility on an active military base under attack. McDonald et al. used a scanning electron microscope to look at propellant samples aged at 100% relative humidity, and he concluded extensive changes in the particle size and morphology of the samples occurred, contributing to a burn rate change in the samples[5]. Changes in the particle size or morphology have been observed in studies of thermally degraded samples, and it is suspected this is the reason for burn rate alterations[5]. While reviewing past research, it seems that a more modern approach could prove to be helpful in enhancing the understanding of effects of high temperature thermal degradation on solid propellants. Optical instrumentation techniques were the decided approach for acquiring the data. Historically, optical measurement techniques have been used to measure the burning rate of solid propellants such as Eisenreich et al. from 1987. While others like Parr et al. have used optical diagnostic techniques to study flame structures[10]. Eisenreich et al. used a photo diode array with a data acquisition system in a Crawford bomb to collects images of the burning solid propellant samples[11]. Optical diagnostics for the study of solid propellant combustion behavior is still in the development stages and requires further development to improve the capabilities of the technology.

To further the understanding of the combustion of thermally degraded solid propellants, an experiment was conducted to measure the time-resolved burn rate of undegraded and thermally degraded propellant samples. The time-resolved burn rate experiment was designed to have used high speed imaging and image processing techniques not previously used, but some issues were encountered. This new technique was validated by comparing it to documented average burn rates of propellants using the classical break wire technique used frequently in past studies[12,13]. After

initial evaluation of data from the updated automated system, the correlation of the data in comparison to historical data was not sufficient for use in the study of the high temperature degradation of the solid propellant. As a result, the final method used was based on a manual selection tool to codify the burning line on the propellant samples and then reduce the data. The frequency of images analyzed is shorter than the automated selection method, but correlates better with historical data from undegraded propellants. This method could be compared to that of the research done by Powell et al. and Thomas et al and can be accomplished in a timely manner, without the need to perfect the automated code.[4,14]. In the literature review it was determined this method is sufficient, and the data of the high temperature thermally degraded propellants was not only of interest to the aerospace community, but also improved the community's understanding of thermally degraded solid propellants for future utilization considerations.

Chapter 3. Solid Propellant Testing Facilities

This research centers on optically measuring the time-resolved burning rate of a thermally degraded and undegraded solid propellant. To this end, repeatable methods for mixing, curing, and thermally aging solid propellant samples were required. To determine the burn rate, measurements of the time variation of the unburned solid propellant surface were taken using a high-resolution, high-speed (~1 kHz) optical images in a high-pressure, optically accessible "strand burner" that incorporated a nitrogen co-flow to purge the pressure vessel of any particulate matter and smoke that would obscure the images. In addition, a ballast tank system was used to prevent the build-up of pressure within the strand burner during the tests. This section describes (1) high-pressure, optically accessible strand burner, (2) mixing and curing, and (3) thermal aging facilities.

High Pressure Strand Burner

For this investigation, the high pressure, optically accessible, constant pressure "strand burner" shown in Fig. 1 was developed. The major components of the optically accessible strand burner include: (1) strand burner body, (2) window retention plate, (3) pressure relief burst disc, (4) burst disk retention plates, (5) the sample holding apparatus, (6) top flow plate, (7) bottom block, and (8) quartz glass window. A nitrogen purge flow system provided for a steady, constant pressure purge flow to prevent the build-up of exhaust gases, and finally, a ballast tank system was used to ensure the pressure vessel remained at constant pressure throughout each test. The details of each of these are described below.

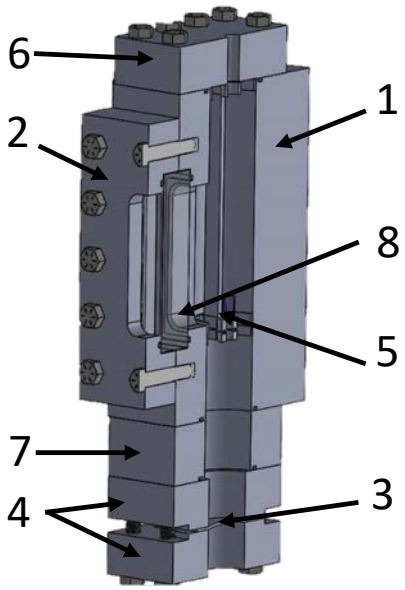

Fig. 1: Cross Sectional View of the Strand Burner Pressure Vessel

An optically accessible pressure vessel was developed to contain the sample and sample holder under high pressure conditions while providing optical access to the burning solid propellant sample. The pressure vessel was designed for a maximum operating pressure of 103.4 bar, and ANSYS structural analysis software was used to ensure a factor of safety of 3 or higher. The body of the strand burner was designed for ease of assembly and strength of design. The test section of the pressure vessel was formed by boring the pressure vessel to a diameter of 76 mm over the entire pressure vessel length of 356 mm. The body was calculated to have a minimum factor of safety (FOS) of 3.1197 as shown in Fig. 2. The strand burner body was machined to create a flat face, which served as a mechanical stop for the window retention plate. The mechanical stop enforced a designed distance to seal the window for proper internal pressure while protecting the window from mechanical failure. The outer pressure vessel geometry was cylindrical due to the

higher strength properties of a circular versus square geometry. To window opening corners were filleted to prevent stress concentrations at these points.

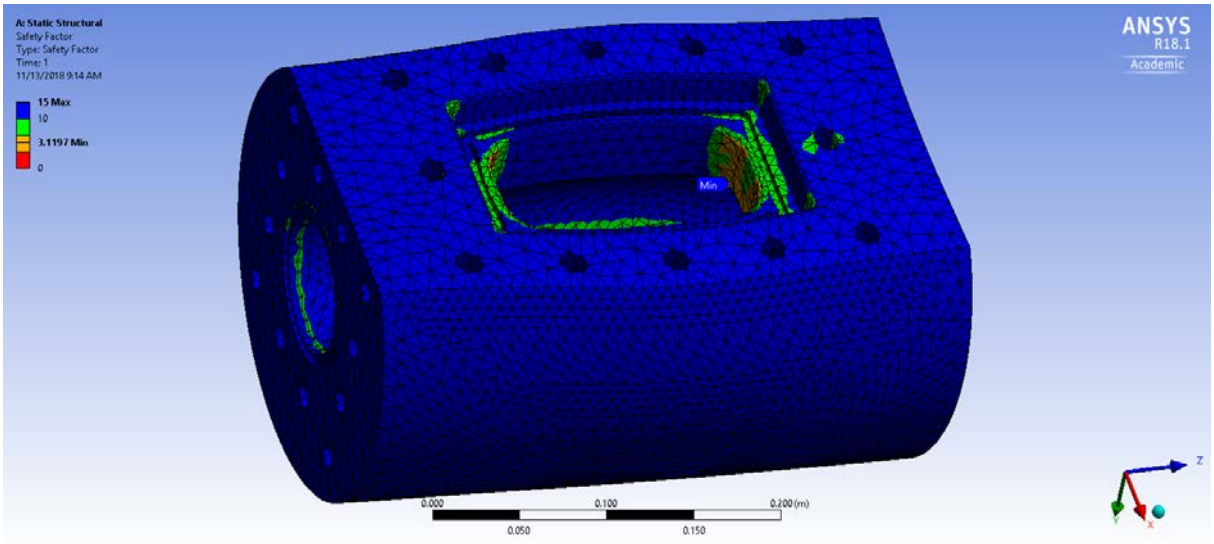

Fig. 2: Ansys Analysis of the Strand Burner Body with the Minimum FOS Marked

The optical access port was created by machining a 2 inch by 4-inch rectangular opening in the side of the pressure vessel as shown. A quartz window was fitted to this opening, and the window was retained by a window clamping plate as shown in Fig. 3 To prevent stress non-uniformity in the quartz window, the window retention was designed to clamp the window with the O-rings to seal against the internal pressure while preventing the quartz window from contacting the metal surface. The window clamping plate was calculated to have a minimum FOS of 6.4451 as shown in Fig. 3, with the location of the lowest FOS flagged as inside the viewport lip. The internal edges were curved in design to limit edge stress, and the bolt pattern was designed to prevent stress concentrations when assembling the strand burner.

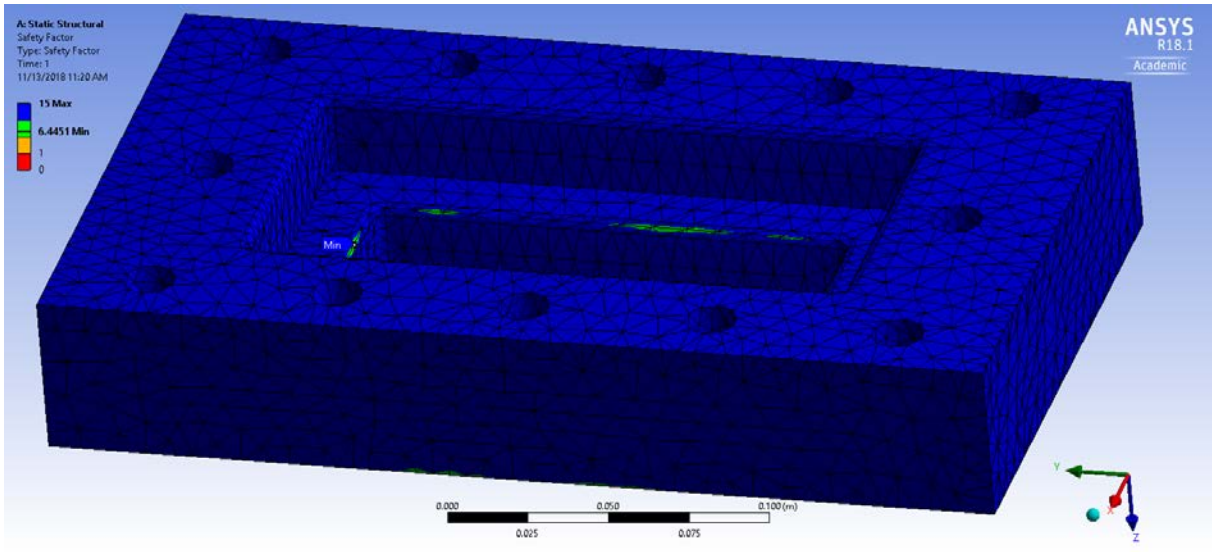

Fig. 3: Window Retention Plate with Minimum FOS Flagged

Optical access was provided in the side of the pressure vessel through a 51 mm x 152 mm window port which was covered using a 191 mm x 89 mm x 44.5 mm thick quartz window mounted on the front face of the pressure vessel as shown in Fig. 1. The quartz window was designed to have a FOS of at least 7, which is suggested by the manufacturer for the quartz windows[15]. The quartz window was designed using clamped edge plate stress theory which was stated by the manufacturer. The thickness, t , of the window is given by

$$x = \frac{R}{r} \tag{3.1}$$

$$k_{clamped} = -0.0179x^4 + 0.2098x^3 - 0.9037x^2 + 1.7002x - 0.6804 \tag{3.2}$$

$$t = \sqrt{\frac{k\,\mathrm{Pr}^2}{(S_{\max})}} \tag{3.3}$$

Where the dimensions of the unsupported portion of the quartz window is represented as R for the longer dimension and r for the shorter dimension. The ratio of the lengths in Eqn. 3.1 is equal

to x and is used to calculate the value of k for clamped windows in Eqn. 3.2. Equation 3.3 uses $k_{clamped}$ from Eqn. 3.2 multiplied by the pressure difference on the window in pounds per square inch (PSI) and multiplied by the shorter dimension of the window squared. This value is divided by the max allowable stress set by the designed factor of safety in PSI, and finally, the thickness is the square root of that value. Equation 3.3 was used to calculate the minimum window thickness required to allow for a factor of safety of 10 at a test pressure of 1500 psi.

The bottom block, shown in Fig. 4, was fitted to the bottom of the pressure vessel to provide in inlet port for the nitrogen purge flow and mounting point for the burst disk assembly described below. This block, shown in Fig. 4, was calculated to have a minimum FOS equal to 6.6726 with the minimum FOS flagged inside the bore on the gas ports. In order to increase the minimal FOS and improve strand burner assembly, the block was redesigned by removing the gas ports, resulting

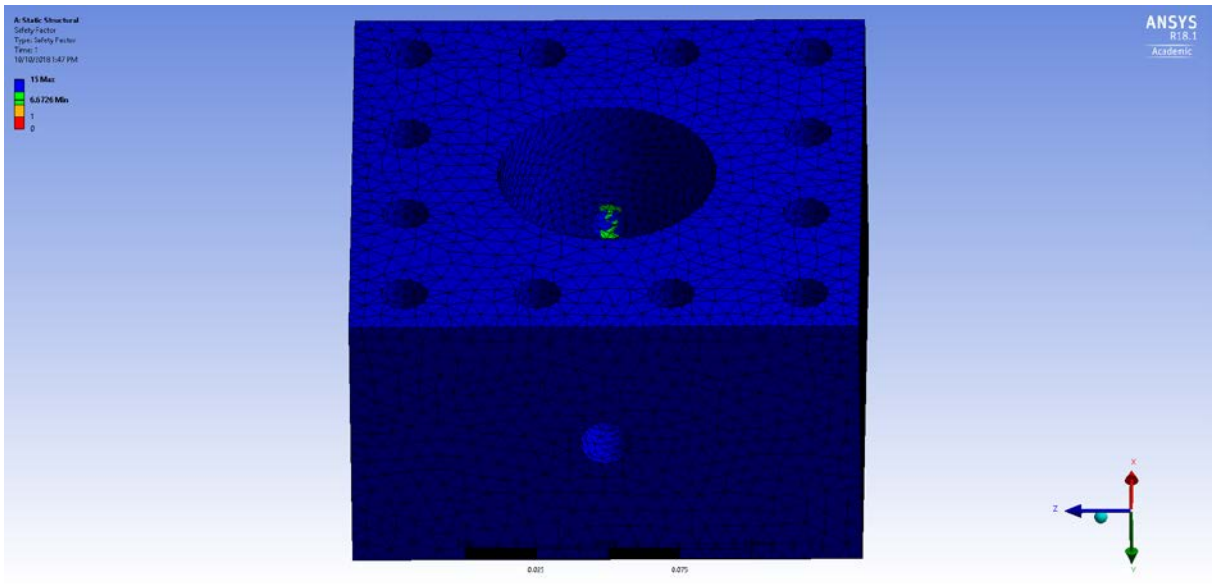

Fig. 4: Bottom Block with Minimum FOS Flagged

in a solid steel spacer. This design created space between the underside of the cart shelf and the strand burner chamber for accessibility of instrumentation and flow ports.

In order to guard against an accidental over-pressure of the pressure vessel, a burst disk assembly was fitted to the pressure vessel below the “bottom block” described above. The burst disk was designed to rupture at 550 psi since the maximum pressure for these experiments was to be 500 psi or below. The burst disk retention plate, shown in Fig. 5, was calculated to have a minimum FOS of 4.3948 and was flagged at the edge of the internal bore at the surface where the burst disk sits. The final design uses two of the burst disk retention plates to hold the burst disk assembly. The upper plate contains ports for instrumentation and flow which are included in the ANSYS analysis. The distribution of the bolts was designed to assist in preventing point loading when assembling the strand burner and to distribute the pressure load.

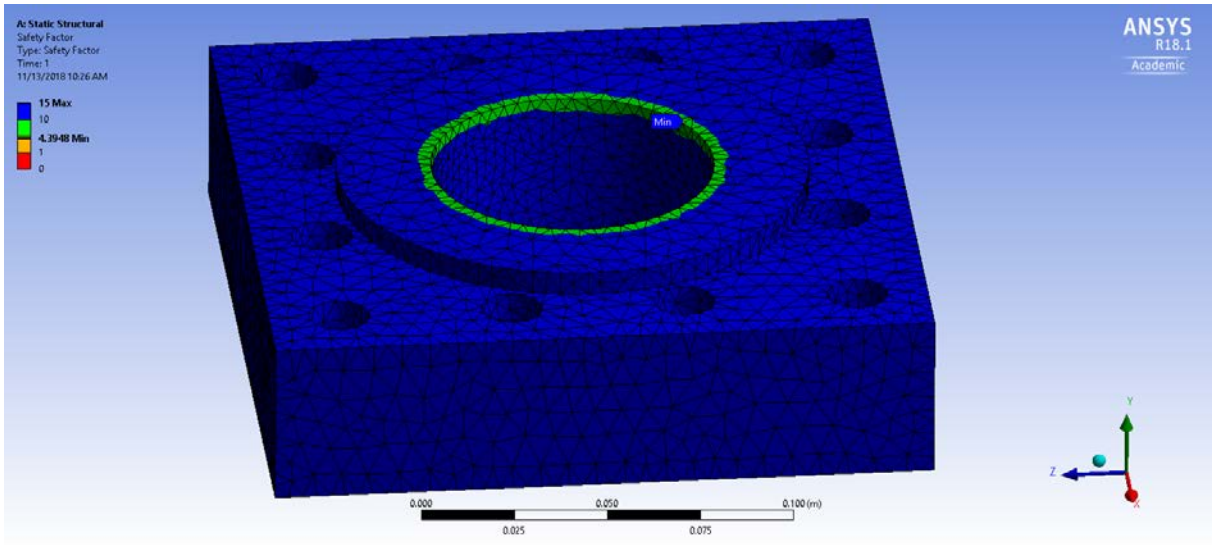

Fig. 5: Burst Disk Retention Plate with Minimum FOS Flagged

The pressure vessel was closed at the top using a “top flow plate”, which also provided a port through which the exhaust and purge gases could escape. The top flow plate, shown in Fig. 6, was calculated to have a minimum FOS of 6.8688 at 103 bar. The minimum FOS occurs at the sharp

lip, which is the port for the outlet of the combustion products and biased flow. This port was made by drilling and tapping a ½" NPT hole in the top plate, so the ANSYS analysis is not able to represent the final product with complete accuracy; however, the NPT fitting did not significantly deviate from the ANSYS analysis. The bolt arrangement was designed for repeatable sealing and

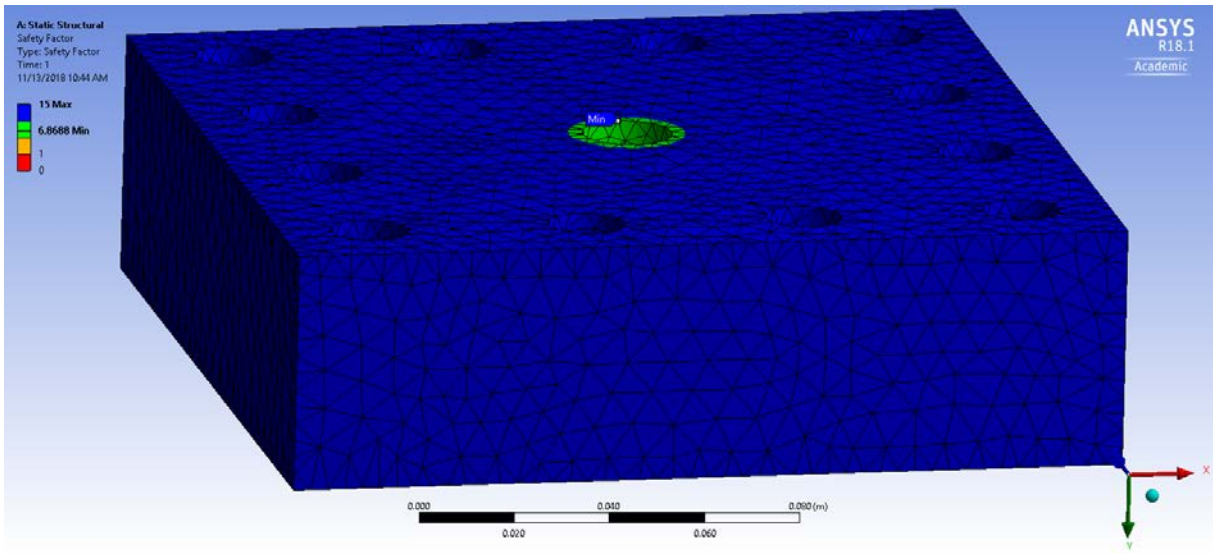

Fig. 6: Top Flow Plate with Minimum FOS Flagged

torqueing to design specifications. The torque specifications were set to 120-foot pounds and were designed for the maximum design pressure with full pressure cycling.

A purge flow of nitrogen gas was used to prevent the buildup of smoke and particulate matter that would tend to obscure optical access. A schematic of the nitrogen supply system is shown in Fig. 7. The nitrogen supply system components were all rated to withstand pressures up to 136 atm.

The nitrogen purge flow leaving the supply system entered the pressure vessel through a port in the burst disk plate at a flow rate of 700 liter per minute (LPM). Tests were conducted to ensure the flow rate was high enough to allow for adequate chamber purging without affecting the

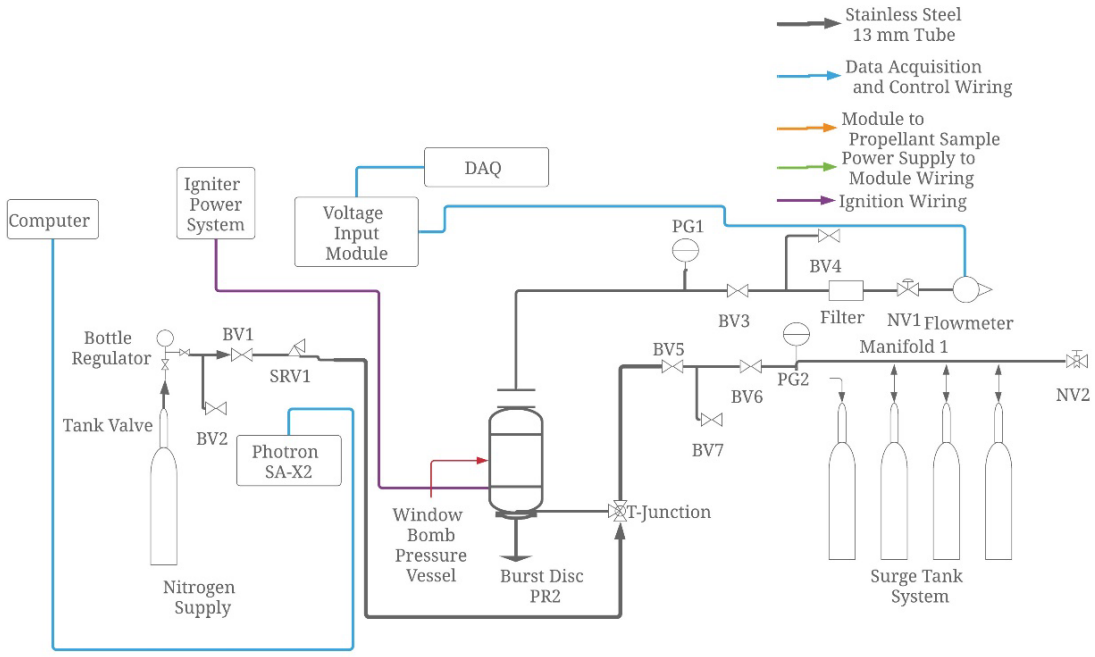

Fig. 7: Full Strand Burner Rig P&ID

combustion of the solid propellant sample. Nitrogen was supplied to the nitrogen flow system by industrial grade nitrogen cylinders, which had an initial pressure of approximately 170 atm. A single stage pressure regulator was connected to the cylinder to provide the nitrogen supply system inlet pressure with a constant pressure of 34 atm. Although the supply cylinder pressure dropped over time, the regulator was able to maintain constant nitrogen supply system pressure and flow rate until the tank pressure reached 34 atm. A 36 atm pressure relief valve and a 38 atm burst disc were used to protect the supply system and pressure vessel from potential overpressure in the event of a regulator failure.

The nitrogen supply tubing from the regulator was connected by a T-junction to both the pressure vessel and a ballast tank system described below to ensure constant chamber pressure throughout the burning process. Upon exiting the T-junction, the nitrogen flowed through the pressure vessel,

past the sample, and out of the exhaust port located in the top flange of the pressure vessel. The exhaust mixture then flowed through a 13 mm stainless steel tube through a 0.2-micron filter, removing particulate matter from the exhaust gas. The nitrogen then flowed through an Omega FLR6725D flow transmitter before flowing through a manual needle valve, for flow control.

The ballast tank system was constructed from three A-size inert gas cylinders connected to each other via a manifold system, utilizing 13 mm stainless steel tubing connected with compression fittings.

The sample was held by a sample holding fixture that also provided the electrical contact points for the hot wire ignition system. The sample holding fixture, see Fig. 8, consists of a 3D printed upper plate with alignment pegs for repeatable sample alignment. The lower plate was also

Fig. 8: Sample Holding Fixture

manufactured using 3D printing and houses the connection points for the electrodes and the magnets which were used for connecting the ignition circuit. The electrodes connected the upper and lower plates and provided the structure of the sample holding fixture. The propellant samples with quartz tube inhibitors described below sat in an indention in the bottom plate which was sized for the quartz tube that was used with the propellant samples. The holding fixture was mounted into the test section by being lowered into the pressure vessel from the top and the sample was aligned with the window and camera using the alignment pegs.

Quartz tubes were used as inhibitors on the exterior of the propellant samples to prevent the grain burning on the sides. Having the samples burn only from the end allowed for some assumptions to be made for the post processing. The main assumption was that the propellant is burning semi-evenly across the face and therefore the burning rate can be calculated as the speed at which that burning line changes versus time. In Fig. 9 the propellant strands can be seen labeled with 1 and the quartz tube sleeves are labeled with 2. The quartz tube did collect soot during the burning process which made the flame shape information impossible to get with this setup.

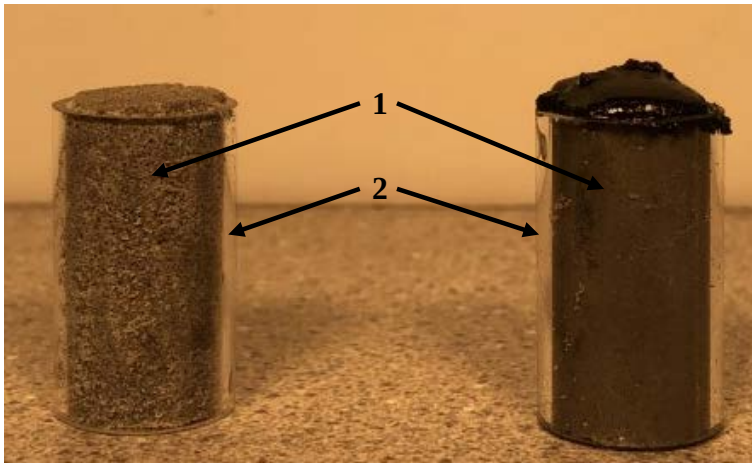

Fig. 9: Propellant Samples in Quartz Tubes

The propellant samples were ignited using an electrically heated nichrome wire embedded in an ignition paste. The ignition paste consisted of a combination of 65% 200-micron AP, 5% copper chromate, 5% aluminum powder, and 25% HTPB. The nichrome wire was heated by an electric current passed through the wire. An example of a propellant sample and the ignition system is depicted in Fig. 10; labeled in the depicture are the locations of the electrodes (1), nichrome wire (2), ignition paste (3), and propellant sample (4). Screws were utilized to attach the nichrome wire to the electrode, pinching the wire against the electrode.

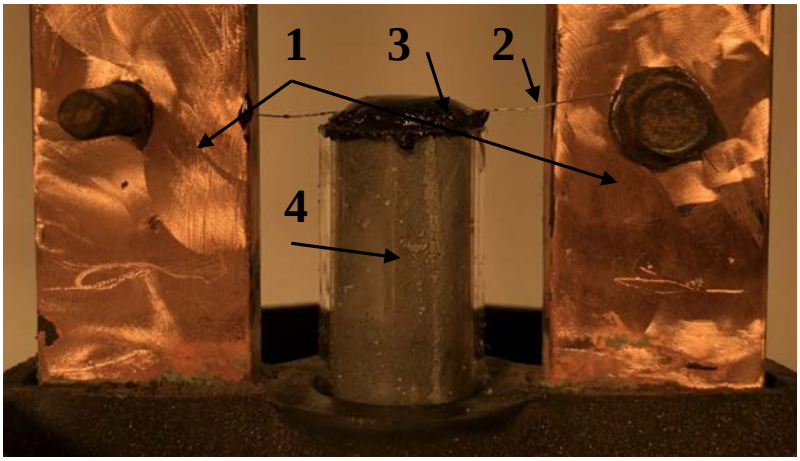

Fig. 10: Sample Setup with Ignition System

Propellant Mixing, Casting, and Curing Facilities

Auburn University's current propellant mixtures are based on a combination of ammonium perchlorate (AP) and hydroxyl terminated polybutadiene (HTPB) with additives such as 30-micron aluminum powder (AL). The current process for mixing and casting propellant utilizes a hand mixing setup, vacuum chamber, and silicone molds.

To start mixing the propellant, the HTPB resin, absent of the curing agent, was added to the mixing bowl. Then the aluminum powder was slowly poured in and mixed thoroughly before the AP was added. At this point, the AP was poured into the bowl and blended into the mixture in the same manner as the AL. After all propellant ingredients were combined the mixture was heated and degasified in the vacuum chamber. The mixtures were degasified for approximately 2 hours each. At that timeframe most of the bubbling had stopped and was considered ready for curative addition. The curative agent was added only after the propellant was mixed, heated, and degasified. This mixing process specifically prevents the mixing of any dry materials, which represents a future significant fire hazard. The mixing was performed in atmospheric condition.

The mixed slurries were poured into the silicone molds one half at a time and pressed together. This method helped to prevent the formation of voids. After adding propellant to the molds, excess propellant was expelled, and the shape of the samples were confirmed by compression of the molds.

Thermal Aging Facilities

The thermal aging process was implemented in a temperature-controlled laboratory oven capable of safe, long-term/extended period operations. The estimated time range for operations ranged from a few minutes to approximately 200 days, mirroring range durations in past thermally aged propellants studies[4]. For this experiment's specific purpose, the degrading process was reduced to 5 minutes. As seen in the study by Thomas, the use of thermal degradation to simulate and codify the aging of a solid propellant is an accepted process quantified and modeled by the Arrhenius equation[4]. It was described as the shelf life, *t*, which can be validated by Eqn. 3.4.

$$t_1 = t_T * f^{(T_t - T_s)/\Delta T_R} \tag{3.4}$$

For this experiment, the propellant samples were kept at an elevated temperature of 265° C for 5 minutes. Based on the final calculations, the artificial age (Shelf Life) of the propellant was approximately 48,000 years. This artificial age is based on the Eqn. 3.4 but does not seem reasonable for these conditions. This study is not claiming that this degradation process produces a propellant that acts to that of a propellant that has aged for 48,000 years, but rather it is focused on the specific conditions of high temperature, short duration thermal degradation. The propellant samples can be seen in the degradation oven in Fig. 11.

Fig. 11: Propellant Samples in the Degradation Oven

Diagnostics and Control

High-resolution, high-speed flame images were captured using a Photron FASTCAM SA-X2 high speed camera. Images were acquired at a rate of 1,000 frames per second (FPS). The initial lens face was approximately 31 cm from the sample utilizing a Nikon 18-55 mm lens with no optical filters. These high-speed flame images provided two significant information elements: (1) the flame structure data as it propagates through the sample; (2) sample burn rate data as a

function of position in the sample and time. Fig. 12 shows an image sample from the high-speed camera of a piece solid propellant burning. In Fig. 12 the piece of propellant was in the middle of the bottom of the frame (label 1). The light intensity was set low as a precautionary measure to prevent the burning propellant from oversaturating the images. The burning line of the propellant (label 2) was measured during the diagnostics. Label 3 denotes the flame exiting the quartz tube. In the downstream flow, glowing particles of aluminum or propellant are depicted in label 4. At some distinct points of the process, the image became obscured; however, this did not have a significant effect on post processing. To prevent image obscuration, increasing the flowrate of the nitrogen flow is recommended in the future processes. The instantaneous burning rate was determined by measuring the difference between the burned propellant area and the area of the unburned propellant.

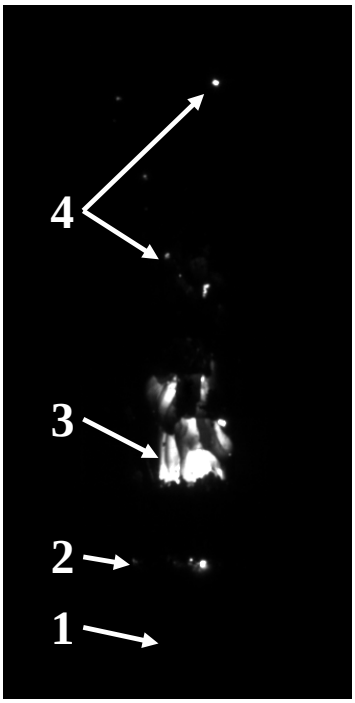

Fig. 12**: Image of Burning Propellant from High-Speed Camera**

Image Processing

The images were processed using MATLAB with automated selection and manual selection of the burning line. The automated selection of the burning line used the intensity values of the individual pixels and created an area where the unburned propellant remained. The images were cropped to a size which was equivalent to the propellant sample size with an additional small margin. Repeatability of sample placement was accomplished as seen with the sample holding fixture from Fig. 8. The cropped images were read into MATLAB and converted into a map of the image intensity values. The study's black and white images facilitated the conversion to intensity values. The images were subjected to a process which began at the bottom left corner of the images, proceeding with each column at a time and generating the code in increments of one pixel at a

time. This methodology was executed until a discovery of an intensity value was greater than or equal to the set value. The burning face of the propellant was labeled with this data. After the location of the burning line, the image was turned into a map of 0's and 1's to calculate the area of the unburned region below the burning line. Throughout the duration of the tests, the quartz tube and propellant were known, and the camera setup did not change; this established a constant base line for conversion from pixel squared area to mm squared area. The findings from the conversion area changed in relative value to the timing data for the assumptions of the end burning face constant area and denoted the conversion to change in length versus time.

Manual selection of the burning line and calculation of unburned propellant area was accomplished in MATLAB using the following steps. Each individual image was run through the algorithm and plotted after the unburned area was calculated. The algorithm included importing the image and cropping the image to the size of the propellant sample. Since the sample size and location did not change across the experiments, the simplicity of the computations was enhanced. Next, the complement of the image intensity values was calculated and saturated at the bottom and top 1 percent of pixel values. The complement of an image was obtained by inverting the intensity values of the original image. This adjustment expedited determination, with the human eye, of the burning line in contrast with the darker images. An example is shown in Fig. 13. Then a region of interest

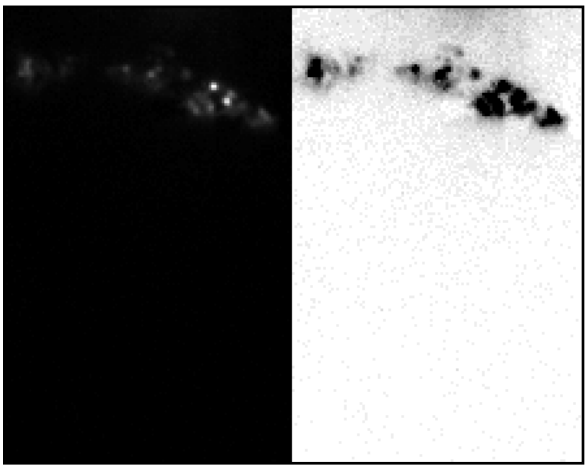

Fig. 13: (Left) Original Cropped Image and (Right) Complement of the original cropped image.

was drawn with a polygon function; from the depicted region of interest, a mask was created. The white image area was measured with a MATLAB function; the specific measurements represented the area of the unburned propellant. An example of the images used for the process is shown in Fig. 14. After the mask area was calculated, the data was used to calculate the unburned area versus time which was accomplished by converting the pixel area to mm area based on the width of the

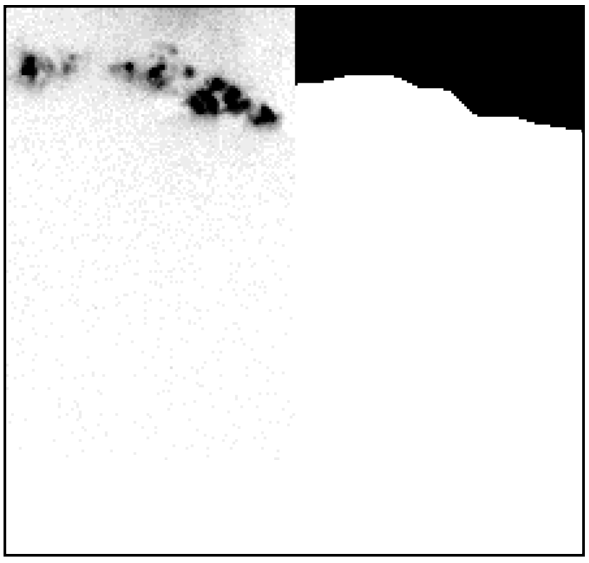

Fig. 14: (Left) Image Used for Selecting Burning Line Manually and (Right) Masked Image

quartz tube and known sample size. The average unburned area versus time was calculated by computing the average at each moment in time and the error bars were the maximum and minimum values at that time. The burning rate was calculated by converting the unburned area change to change in length by using the known length of the sample and using a conversion factor. From there the slope of the unburned area line was calculated with the equation and conversion factor given by

$$BR = \frac{\frac{BW_{i+1} - BW_i}{X_{i+1} - X_i}}{111} * \left(\frac{25.4}{175} \right) \tag{3.5}$$

and the burning rate versus time was plotted. The equation used to calculate the burning rate is shown in Eqn. 3.5. in the burning rate equation BR is the burning rate in mm/s, BW is the unburned area of the propellant in pixels squared at the i^{th} position, and X is the is the time in seconds at the i^{th} position. The conversion from pixels squared per second to millimeter per second is accomplished with the ratio of pixels to millimeters in the long dimension of the propellant sample and also the number of pixels across the propellant sample. Other values such as the standard deviation of the burn rate plots was taken from a MATLAB analysis tool of the plots.

Chapter 4. Experimental Description

The experiment execution can be described in two parts: the preparation of the propellant samples and the testing of each propellant sample. Comprised of the same three elements, a solid oxidizer, a solid fuel, and a liquid polymer binder, each of the six batches of propellant samples varied in the element percentages to observe the effect of degradation. When the propellant production and degradation were complete, testing within the high pressure stand burner began and image data was collected. These images were later analyzed through MATLAB to extract the burning rate of each propellant formulation and degradation.

This section describes experiments executed in the strand burner apparatus. All described experiments utilized ammonium perchlorate (AP), hydroxyl-terminated polybutadiene (HTPB), and aluminum (AL) powder solid propellant samples. A specially designed fixture secured the propellant sample in place and aligned the sample with the window. The test pressure was set at 500 psi for the experiments. Prior to each test, the sample was positioned in the strand burner and the exhaust orifice adjusted to the desired diameter. The nitrogen bias flow was then initiated, and the chamber pressure allowed to equalize to the desired test pressure. Upon reaching the desired chamber pressure, the sample was ignited with the electronic ignitor and the data acquisition system was initiated.

The burn rate experiments used cylindrical samples with quartz inhibitor sleeves. The cylindrical samples measured 17 mm in diameter and approximately 25 mm long.

In this series of tests, a range of propellant mixtures was measured for burn rate and flame characteristics. The propellant composition was tested by altering the percentages of AP, HTPB, and aluminum powder. The tested propellants utilized the compound mix of 30-micron aluminum powder, 200-micron AP, 30-micron aluminum powder, and HTPB with a 0.80 OH value. The first set of tests was implemented, shown in Table 1, with a material mixture of 60% AP, 30% HTPB, and 10% aluminum powder. The propellant chemistries with the respective curing date method are

Table 1: Propellant Chemistries with Curing Date and Method

Propellants	AP	HTPB	AL	Date	Cure Method	Cure Time
1	60	30	10	3/23/2020	60℃	2hr
2	65	25	10	3/22/2020	60℃	2hr
3	65	30	5	3/26/2020	60℃	2hr
4	60	40	0	3/22/2020	60℃	2hr
5	65	35	0	3/25/2020	60℃	2hr
6	70	30	0	3/23/2020	60℃	2hr

shown in Table 1. The measured burning rate was the basis for Eqn. 4.1 where r_1 is the burning rate, p is the pressure, a is the empirical temperature coefficient, and n is the empirical pressure coefficient[16]. Solid propellants burn slower at lower pressures as stated with Eqn. 4.1.

$$r_1 = ap^n \tag{4.1}$$

These tests provided data on burn rate variation for a wide range of propellant mixtures and established a baseline to compare with subsequent tests. Fig. 15 displays a sample of the images from the MATLAB image processing for codifying propellant burning rates. The image set is from a data set of propellant 6. The burning line is seen in the left image of Fig. 15 when the propellant changes from bright white to black. Also, this can be seen in the right image lower in the picture as the propellant has been burning for a period of time. As discussed above, the high-speed camera recorded the flame throughout the burn to provide time-resolved flame propagation data. These data were used to determine the test burn rate variation and overall burn rate for the sample.

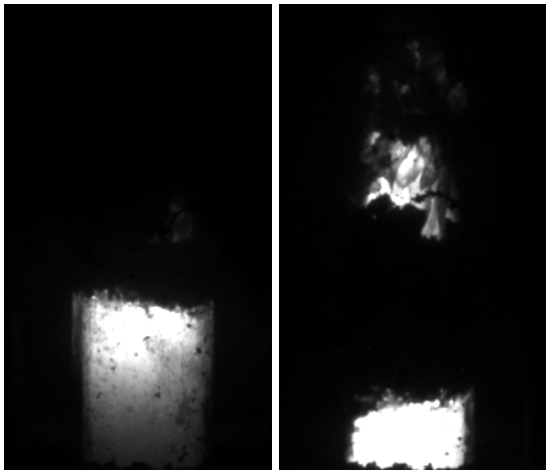

Fig. 15**: Propellant 6 Burning at Two Different Points in Time During a Single Experimental Run**

Error Analysis

This section discusses the sources of error and provides an analysis of the magnitude of these errors for (1) propellant mixing, (2) thermal degradation, (3) purge flow rate, (4) burning line determination, and (5) burn rate calculation. The uncertainty of a measurement is given by

$$u = \sqrt{\frac{\sum \left(x_i - \mu \right)^2}{n^* \left(n - 1 \right)}} \tag{4.2}$$

where the i[th] value in the data set is x_i, the mean of the data set is μ, and n is the number of readings in the data set. The uncertainty, u, for an average value can be calculated using Eqn. 4.2[17]. For example, if the data set was 3,4, and 5 the average would be 4 the number of readings would be 3 and the uncertainty would be equal to 0.57735.

The mixing of the propellant was a source of error to the experiment. The propellant chemistries were based on the mass percentage of the total components. Measured using a digital scale with a precision of 0.1 grams. When looking into the rounding procedure of a typical digitally displayed measurement, if the display reads 30.1 grams then due to rounding the actual value could be in the range of 30.06 to 30.14. Therefore, propellant component mass could be measured to an accuracy of $\pm$ 0.1 grams. The uncertainty of the total of the component masses is given by

$$\%\text{error in total mass} = \frac{m_1 + dm_1}{m_{tot}} + \frac{m_2 + dm_2}{m_{tot}} + \frac{m_3 + dm_3}{m_{tot}} - \frac{m_{tot}}{m_{tot}} = \frac{dm_1 + dm_2 + dm_3}{m_{tot}}$$
$$= \frac{0.1 + 0.1 + 0.3}{100} = 0.3\% \qquad (4.3)$$

and leads to an uncertainty in the overall propellant formulations with a maximum of $\pm$ 0.3% when mixing 100 grams of material based on Eqn. 4.3[17].

The time and temperature control of the curing and degradation oven was also a source of potential error in the final data. The timing of the thermal degradation was kept using a simple stopwatch. While a stopwatch can be precise to $\pm$ 0.01 second, the method of timing the degradation was to start the timer after closing the oven door and then removing the samples at the sound of the alarm. Based on these actions being performed manually, it can be assumed that the timing of the

degradation had an uncertainty closer to $\pm$ 10 seconds. The degradation cycle was operated twice during the course of the experimentation, which is not an amount that is statistically relevant. The uncertainty of $\pm$ was decided based on the knowledge that it took a few second to insert and remove the propellant samples along with starting and stopping the timer. The effect of this amount of time would not have significantly altered the results as the purpose of the study was to observe the effect of the degradation technique used to simulate a real-life scenario. The reason why this uncertainty does not alter the end measurements is that the pinpoint timing of the degradation is not as important as understanding how the propellants react to a thermal degradation scenario that is within a small percentage of the 5-minute thermal degradation timeframe. Additionally, the oven thermal probe measured temperature to 0.1 degrees Celsius. This meant that the temperature measurement of the oven had an uncertainty value of $\pm$ 0.1, which is a low error when operating at 265 degrees Celsius. At 265 degrees Celsius the full-scale error would be 0.04%.

The target nitrogen flow rate was 25 cubic feet per minute as measured by a digital flow meter. The digital flow meter had a precision of 0.01 cubic feet per minute. This produced and uncertainty of $\pm$ 0.01 cubic feet a min on each reading. Based on the manufacturer's specifications the flow meter used had an accuracy of $\pm$2% and a repeatability of $\pm$0.5%. The measurement of the flow rate was 25.09 $\pm$ 0.45 cubic feet per minute with a confidence interval of 95%. With a 95% confidence interval equaling $\mu \pm 2 * u$, where μ is the average measured flowrate and u is the uncertainty value. The nitrogen flow rate was not observed to have an effect on the burning characteristics over the range tested.

The cropping of the raw images and selection of the burning surface location was a portion of the data analysis which added error to the burn rate calculations. The raw images were cropped to be

the size of the quartz inhibitor sleeves, which was approximated by using pixel dimensions of 175 by 111 pixels giving a total pixel count of 19425. The vertical movement of the propellant samples were completely constrained, but the sample holder assembly could move 1 mm either way within the pressure vessel. Based off observations the horizontal uncertainty was $\pm$ 7 pixels for the location of the propellant in the cropped image. The horizontal position determines the amount of the propellant sample that is visible after the cropping of the raw image. If the full propellant sample is not in the view of the pre-determined cropping location, the calculated unburned area would not be across the entire sample and could affect the final burn rate calculation. This error would propagate into the manual selection of the burning line as the propellant could be shifted from sample to sample. The potential for the horizontal location error was minimized by selecting a size of the cropped image that is larger than sample needs by half a millimeter. With the added distance of the quartz sleeve it was observed that the propellant sample was always within the cropped image field. The manual selection of the burning line was a source of error as the burning line was not selected in every column of data as the automated code method, but the burning line selection points were connected with lines that would span across a portion of the columns of data. By the best estimations it was assumed that the uncertainty was $\pm$ 5 pixels at the selection points and $\pm$ 10 pixels at selection line segments that cross multiple columns of data. This error was not capable of being lessened with the manual selection technique, and it can be expected that the error was propagated into the burn rate measurement.

The burn rate measurement is the calculation that accumulates the errors or uncertainties from the entire experimentation process. The average burning rates of the propellant formulations and the uncertainty values associated with the formulations are in Table 2. The data in Table 2 shows another interesting point: across all propellant formulations a higher degree of uncertainty is noted in the degraded samples as compared to the undegraded propellants. The highest level of uncertainty was around 40%, but for most of the propellant formulation the level of uncertainty was between 5-10%.

Table 2: Average Burning Rates of Propellant Formulations and the Associated Uncertainty Values

	Propellant	1	2	3	4	5	6
Undegraded	Average	-1.79	-3.12	-2.19	-1.14	-2.08	-3.33
	Uncertainty	0.08	0.54	0.07	0.04	0.04	0.03
Degraded	Average	-2.16	-3.44	-2.47	-1.58	-2.04	-2.03
	Uncertainty	0.34	1.37	0.22	0.10	0.13	0.46

Chapter 5. Results and Discussion

Post experimentation, analysis of the image data began. Break wire analysis was performed in order to understand and verify with past studies the base line burn rate of the propellant formulation. Another way to verify the accuracy of the experiment was comparing the results of the manual and automated MATLAB codes. These outcomes dictated the decision to use the manual MATLAB code method for the duration of the analysis. Lastly, after the data was quantified, statistical examination allowed for the results of the experiment to be further discussed and for conclusions to be solidified. Intermediate experiments were developed and executed to capture an understanding and relative value comparisons for the final set of experiments. These intermediate experiments were conducted in an atmospheric strand burner to understand what processes would work best in the high-pressure strand burner. These experiments included a break wire setup and optical diagnostic techniques similar to those used with the high-pressure strand burner. Before any optical measurements were taken in the atmospheric strand burner, a simple break wire test was installed and used. An example of the data from that test is, shown in, portraying the voltage versus time data. The data for the second break wire had interference in the first ten seconds; however, the sharp decrease in voltage followed by constant zero voltage confirmed the interference break slightly past 20 second mark. Initial results from atmospheric

conditions for a burn rate experiment targeting a negatively thermally degraded sample are seen in Fig. 16.

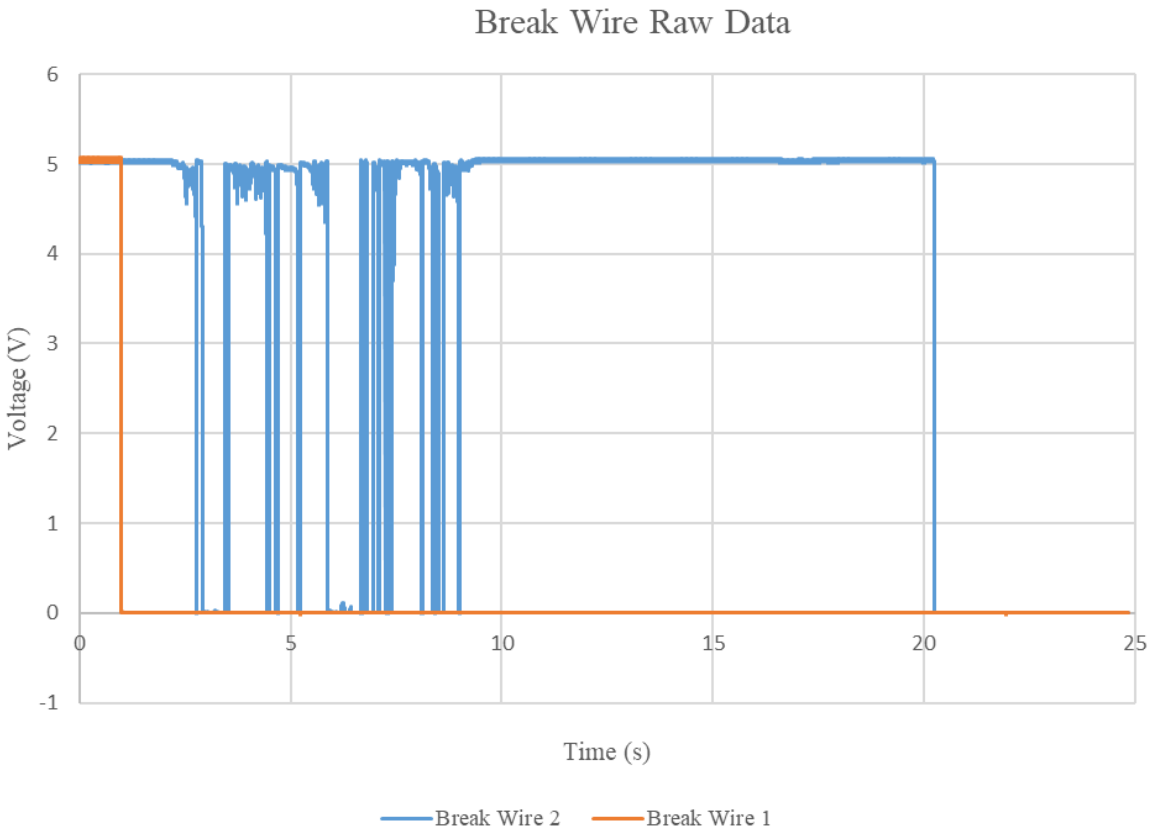

Fig. 16: Example of Atmospheric Conditions Break Wire Data

The burn rate is calculated as the time at which a second break wire goes to zero volts minus the time at which the first break wire goes to zero volts, then it is divided over the known distance between the two. The results from this experiment can be seen in Table 3 establishing the overall burn rate as 1.32 mm/s. These results are in good agreement with past studies[18]. Optical measurements are 136% of the break-wire results and the difference can be attributed to the chamber pressure difference.

Table 3: Initial Burn Rate Data

Wire 1 Break Time (s)	0.99
Wire 2 Break Time (s)	20.25
Change in Time (s)	19.25
Distance Burned (mm)	25.4
Regression Rate (mm/s)	1.32

As the automated code was being considered the comparison of the automated selection code to the manual selection code was important to see if it was a viable method. If the automated code was similar to the manual selection code, then it would have been the choice for data analysis for this study. After comparing the results, it was determined that the automated burning line selection code was not accurate enough in comparison to the manual selection code. The manual selection code was selected for the remainder of the analysis for this study as it was more capable of the developing the understanding of the thermally degraded propellant burning characteristics with less error. Fig. 17 compares manual and automated techniques for the purpose of understanding and deducing the benefits of an automated image processing versus manual image processing.

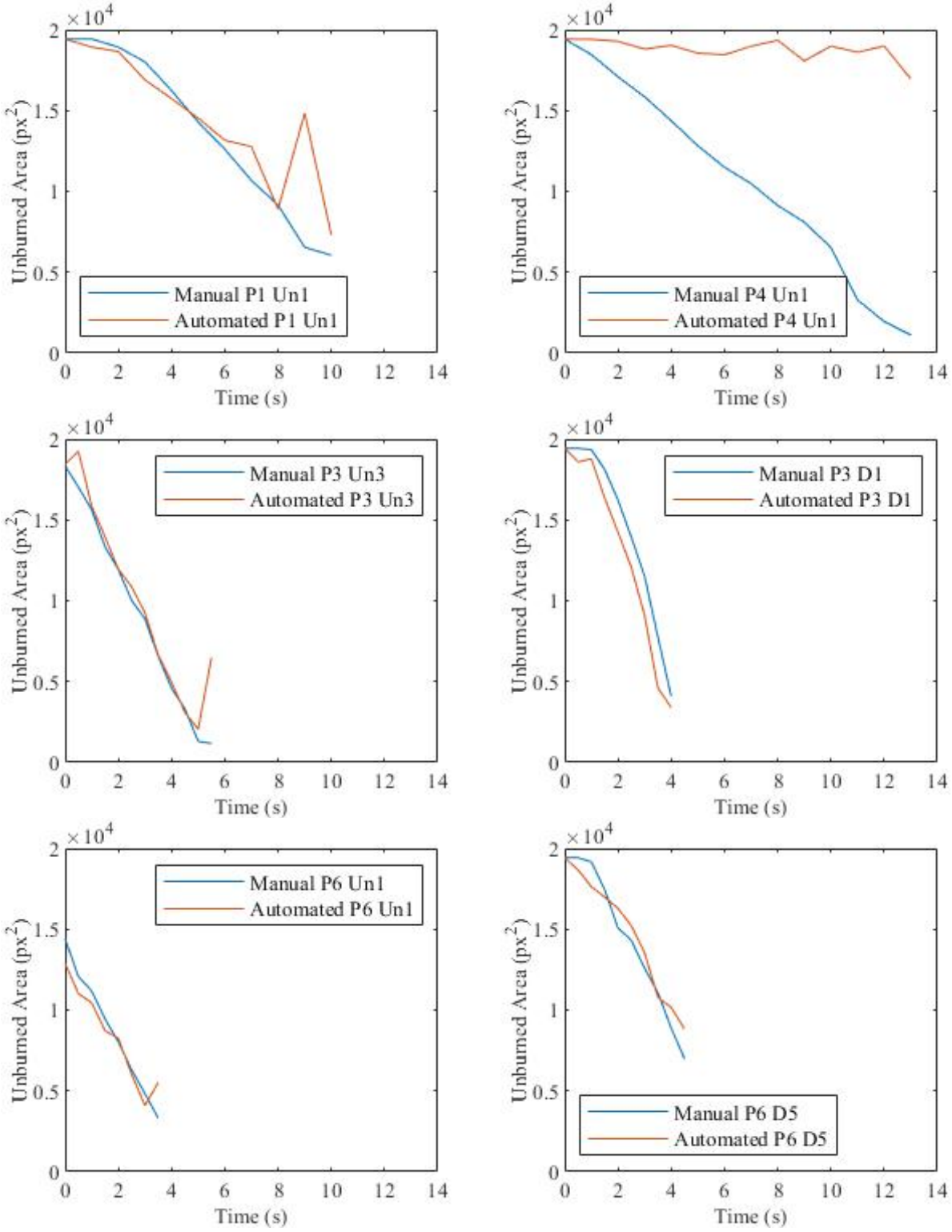

Fig. 17: Comparison Plots of Manual Image Processing to the Automated Process

The automated, time-resolved method has the capability to process thousands of images in minutes, while manual techniques would take days to weeks to process the same size data set. Table 4 displays the overall average burning rates of the propellant using the automated and manual selection techniques. The data shows that the automated selection code was getting close to the manually selected burning areas. At this point for the study, it was determined the manual technique, with a lower time resolution was more repeatable. The automated burning area selection code is revisited in future solid propellant research. Fig. 17 data validate this decision to use the manual selection technique for the study. The automated selection was close in accuracy for a majority of the sample propellants, but the frequency of erroneous data led to more errors in the final analysis.

Table 4: Average Regression Rate of the Tested Propellants

	Manual	Auto Code	Manual/Auto Factor
P1 U1	-1.63	-1.34	1.21
P3 U3	-3.80	-2.64	1.44
P3 D1	-4.66	-4.87	0.96
P4 U1	-1.71	-0.23	7.42
P6 U1	-3.86	-2.56	1.51
P6 D5	-3.36	-2.86	1.17

Observations during experiments are a part of developing the total understanding of what is occurring during the thermal degradation process. In this set of experiments, noticeable differences were observed, and these observations led to some speculation on the factors that were changing the burning rates of the propellant samples.

Visual comparison of undegraded versus degraded propellants is shown in Fig. 18. It is shown that the degraded propellant showed signs of deterioration with samples expanding and discoloring after thermal degradation in the oven at 265° C for 5 minutes. The propellants expanded up to 40% of the original sample size based on an increase in length. The discoloration is believed to be due to a break-down of the polymer binder, which was HTPB. Additionally, differences between the degraded and non-degraded propellant were observed visually with changes in size and color. Although every propellant sample no matter the composition appeared darker post degradation, the propellant without aluminum was significantly darker in comparison to the propellant with

Fig. 18: Undegraded Samples vs. Degraded Samples

aluminum. Also, the propellant without aluminum experienced up to a 40 percent volume expansion resulting in reduced propellant density.

The burn rate of solid propellants is heavily dependent on the rate of heat transfer from the flame to the unburned propellant[19]. Assuming that the primary effect of the color change is on the rate of absorption of radiant energy emitted by the flame, we expect a lighter colored propellant to heat and burn slower than a darker one, and we would expect a lower density propellant to heat and burn faster than a higher density propellant. In other words, for a lighter colored degraded propellant having the same density as the undegraded propellant, the rate of absorption of radian energy is lower for the degraded than for the undegraded case. Therefore, we expect the degraded propellant to heat and burn more slowly than the undegraded propellant.

For a degraded propellant having the same color as the undegraded but with reduced density, we would expect the propellant to heat and burn faster than the undegraded. For degraded propellants having lighter color and reduced density, these effects oppose each other so that whether the burning rate increases or decreases depends on the relative magnitude of these two effects.

Further analysis or experimental investigation into the density and radiant properties would be required to quantify these effects. However, these observations lead to a speculation that this could also be a contributing factor towards the changes in burning characteristics.

After the manual burning line selection technique was determined to be the best method for the analysis, the data was processed for comparison of the degraded samples against the undegraded samples. The information used to compare the propellants included the unburned area of the propellant versus time, the average unburned are of the propellant versus time, and the burning

rate versus time. From this data different conclusions could be made concerning the propellant with a conclusion that there is a change in the burning characteristics of solid propellants that are subjected to a high temperature, short duration thermal degradation process.

The results of the experiments analyzed by the manual selection technique include 6 propellant chemistries, 2 degradation situations, and 5 samples with each propellant chemistry and degradation configuration. The data were separated into two distinct propellant categories for easier analysis: propellants with AL and propellants without AL. Generally, the thermally degraded propellant samples displayed an increase in burning rate. Additionally, it was discovered there was a level of instability in the burning rate with the thermally degraded propellant samples. The degraded propellants did not have a consistent and steady burning rate during the burning period and will be discussed later in the text.

The subplots of Fig. 19 display the area of the unburned propellant versus time for propellants with AL. These data depict the change in burning rate versus time. Undegraded Propellant 1, Fig. 19(a), had consistent and similar burning profiles across all samples. The ignition transient was seconds into the plot, with a shallower graph slope occurring while the burning was reaching a steady state. Undegraded Propellant 1 had a high level of repeatability in the results, however, sample 5 was removed from the data set as a bulk of the imaging was obscured, voiding the findings for data analysis. Degraded Propellant 1, Fig. 19(b), samples exhibited a high degree of fluctuation in regression rate throughout the burn period. The degraded propellant samples overall burning rate was higher than the undegraded samples. This result compares well to results from the past literature. However, the erratic nature of the burning was an unexpected discovery. This erratic burn nature/behavior in a rocket motor could easily lead to instabilities or unexpected stress on the

motor casing. Propellant 2 undegraded and degraded, Fig. 19(c-d), were difficult to process as the propellant did not burn evenly during most experiments but could be seen to burn faster than all other propellants. Propellant 3, Fig. 19(e-f), burned well for both sets of experiments and was easier to analyze with the image processing. The findings lead to the following conclusions: the undegraded samples show higher levels of erratic burning for this propellant chemistry, but the overall burning rates still show the degraded propellants have an increased burning rate.

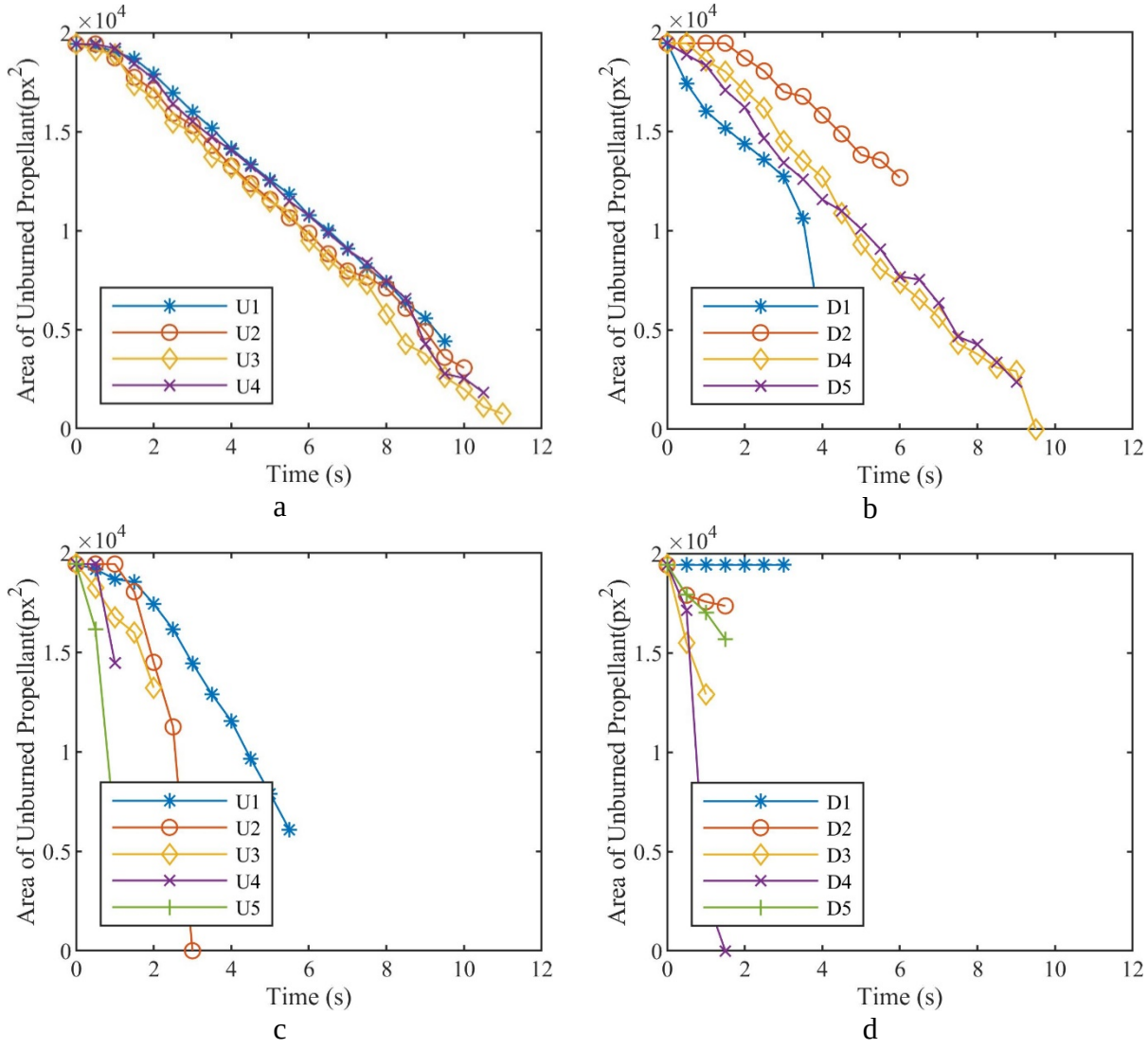

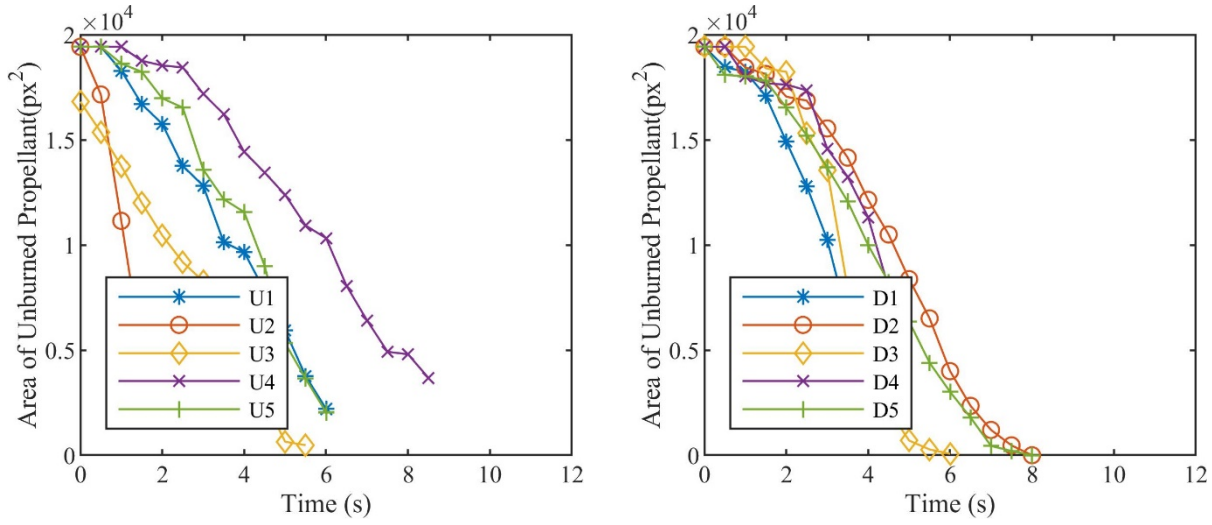

Fig. 19: Unburned Area of Propellant vs. Time for Propellants with Aluminum; a and b are Propellant 1, c and d are Propellant 2, and e and f are Propellant 3

The plots of Fig. 20 display the area of the unburned propellant versus time for propellants without AL. Propellant 4 undegraded, like propellant 3, displayed slightly more erratic burning in comparison to the degraded counterpart and exhibited overall increased average burning rate. Propellant 4 is shown in Fig. 20(a-b). Propellant 5 undegraded, Fig. 20(c), had very consistent burning profiles, while the degraded samples of Fig. 20(d), have overall similar averaged burning rates, but more erratic burning behavior. In several instances, Propellant 5 imaging data was not useful for image processing and had to be removed from the data set. Some of the samples in the propellant 5 data set had unnoticeable gaps between the propellant and the inhibitor sleeve that directed the burning surface down the gap. Any samples that had unnoticeable gaps between the propellant and inhibitor sleeve noticed through burning behavior were removed from the sample set. Propellant 6 displays a reduced data set, as the other samples in the set were not capable of being analyzed due to uncontrollable actions during the burning of the samples. Propellant 6, Fig. 20(e-f), also show the degraded samples burning with slightly more erratic behavior, but the

overall averaged burning rates were slower in the degraded samples; this reaction is validated due to unforeseen issues with the burning of the sixth propellant chemistry.

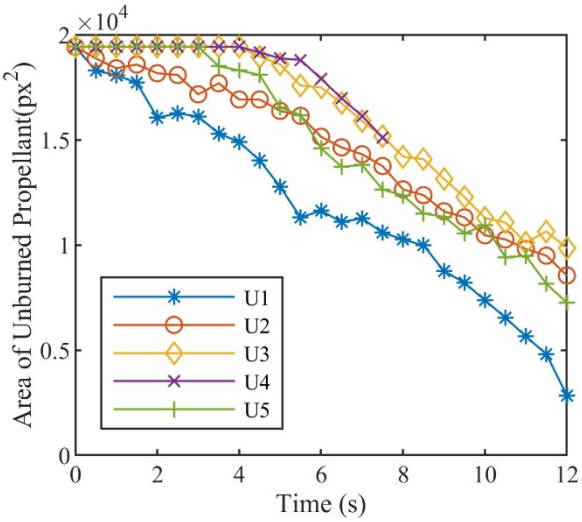

a

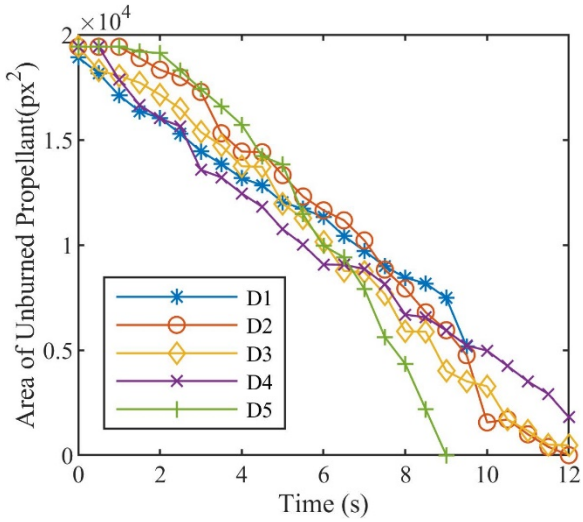

b

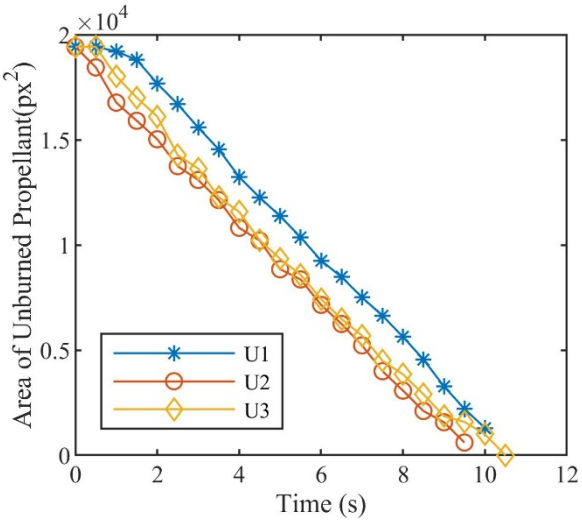

c

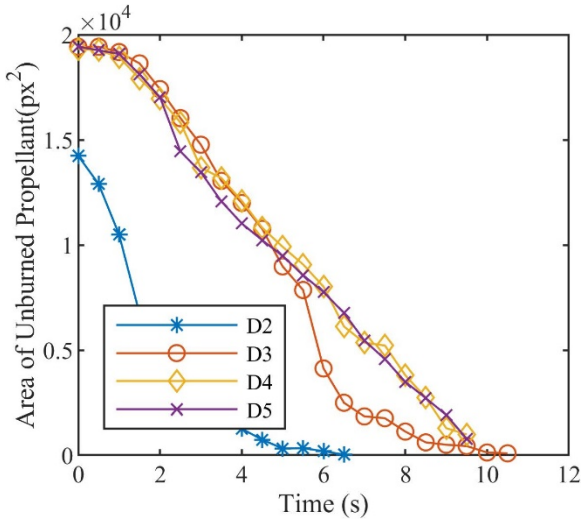

d

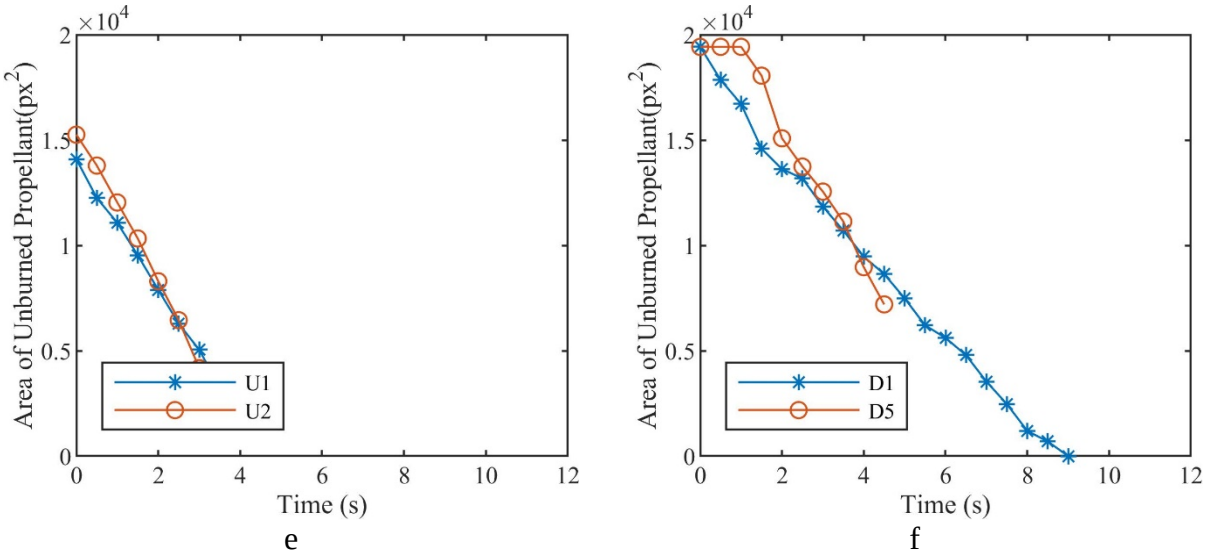

Fig. 20: Unburned Area of Propellant vs. Time for Propellants without Aluminum; a and b are Propellant 4, c and d are Propellant 5, and e and f are Propellant 6

Fig. 21 shows a plot of the average unburned area of propellants 1, 2, and 3 with the limits of the data and assists in showing the erratic burning behavior of the propellants. Propellant 1 undegraded, Fig. 21(a), shows that the area of the unburned propellant decreased monotonically with nearly constant negative slope. The relatively small error bars indicate the high degree of repeatability that was observed in the burning of each of the propellant samples. While the degraded version, Fig. 21(c), portrays an inconsistent average with larger data limits. Propellants 2 and 3, Fig. 21(d-f), show that the degraded propellants had more constant negative slopes in comparison to the undegraded. The relatively small error bars indicate a level of repeatability within the propellant configuration.

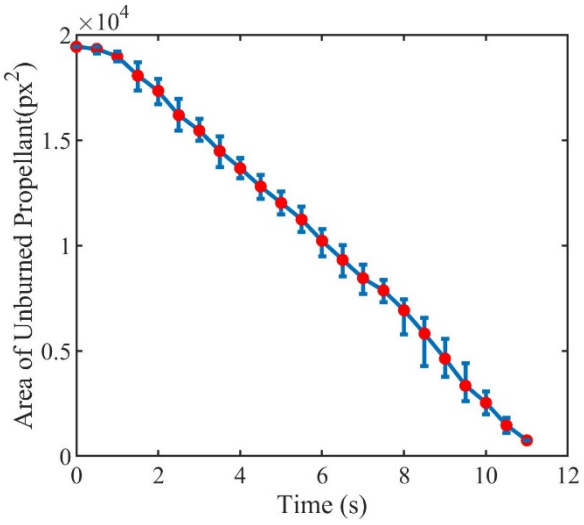
×10^4
Area of Unburned Propellant(px^2)
Time (s)

a

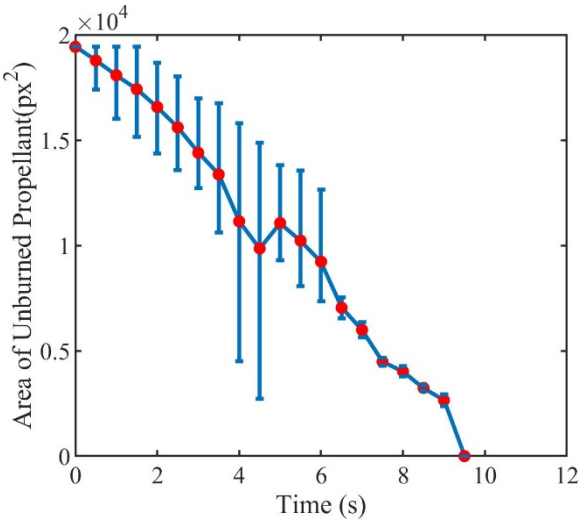
×10^4
Area of Unburned Propellant(px^2)
Time (s)

b

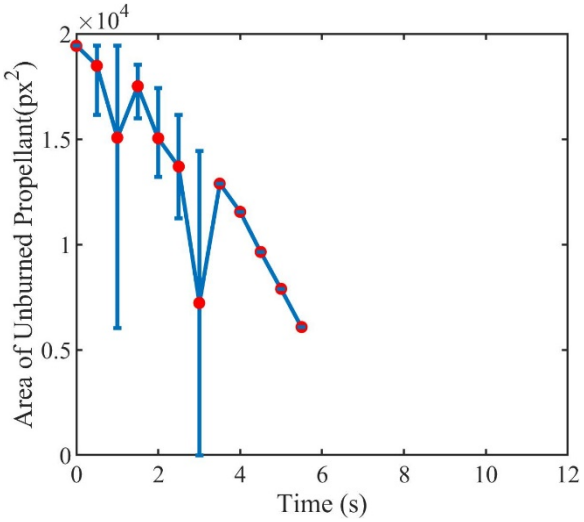
×10^4
Area of Unburned Propellant(px^2)
Time (s)

c

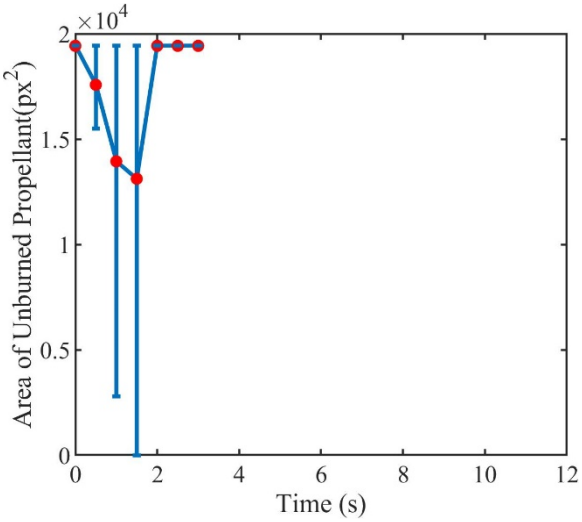
×10^4
Area of Unburned Propellant(px^2)
Time (s)

d

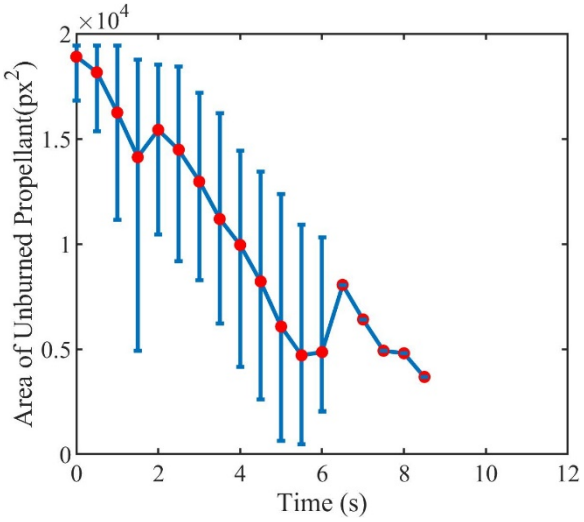
×10^4
Area of Unburned Propellant(px^2)
Time (s)

e

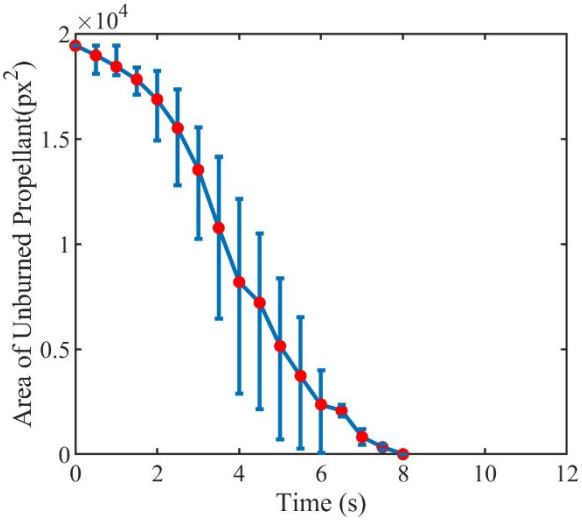
×10^4
Area of Unburned Propellant(px^2)
Time (s)

f

Fig. 21: Average Area of Unburned Propellants with Aluminum Versus Time with Data Limits for the Deviated Unburned Area Data from the Average

The average area of unburned propellant for Propellant 4, Fig. 22(a-b), display more erratic burning behavior from the degraded samples with an inconsistent average unburned area line with the degraded variation having 125% of the standard deviation on the burning rates. Propellant 5, Fig. 22(c-d), undegraded samples burning rates having a higher consistency as compared to the degraded counterparts. Propellant 6, Fig. 22(e-f), degraded burning rates had a 98% difference in the standard deviation of the undegraded counterpart.

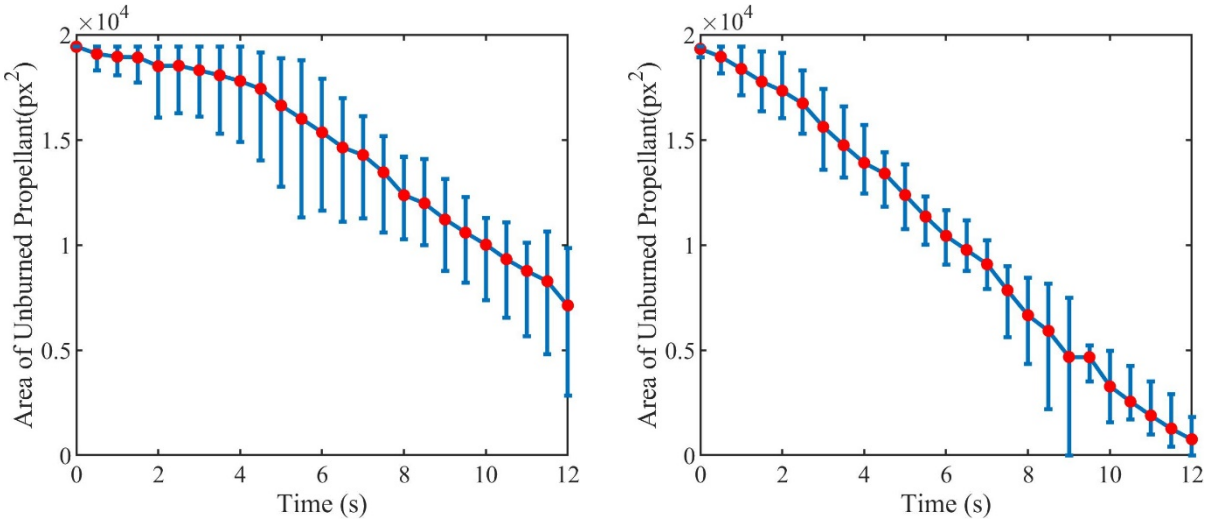

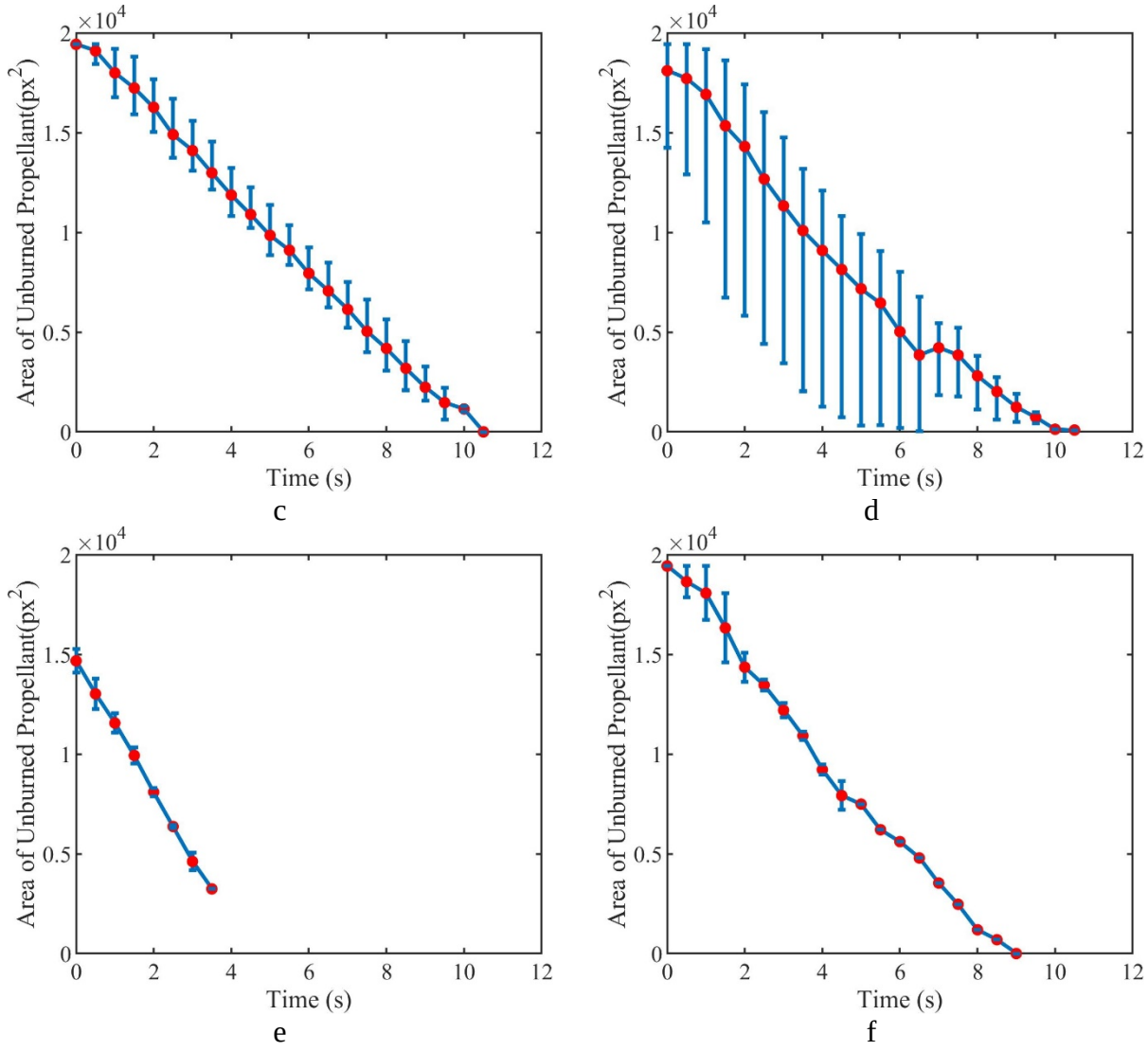

Fig. 22: Average Area of Unburned Propellants without Aluminum Versus Time with Data Limits for the Deviated Unburned Area Data from the Average

Fig. 23 shows the burning rate versus time for propellants with aluminum with an interval of calculation at a half second. All propellants in this data set have negative burning rates throughout the experiments. Constant burn rate would be represented as a horizontal line on a burn rate versus time plot. The burn rate of undegraded propellant 1, shown in Fig. 23(a), exhibits near constant burn rate with a standard deviation of 1.08 mm/s and an average burn rate of -1.79 mm/s. The burn

rate of degraded propellant 1, shown in Fig. 23(b), had a standard deviation of 2.10 mm/s and an average burn rate of -1.82 mm/s. The degraded variation of propellant 1 had a higher average burn rate and higher standard deviation. The burn rate of undegraded propellant 2, shown in Fig. 23(c), had a standard deviation of 5.24 mm/s and an average burn rate of -2.33 mm/s. The burn rate of degraded propellant 2, shown in Fig. 23(d), had a standard deviation of 6.77 mm/s with an average burn rate of -2.76 mm/s. The burn rate of undegraded propellant 3, shown in Fig. 23(e), had a standard deviation of 2.96 mm/s and an average burn rate of -2.19 mm/s. The burn rate of degraded propellant 3, shown in Fig. 23(f), had a standard deviation of 2.82 mm/s and an average burn rate of -2.47 mm/s.

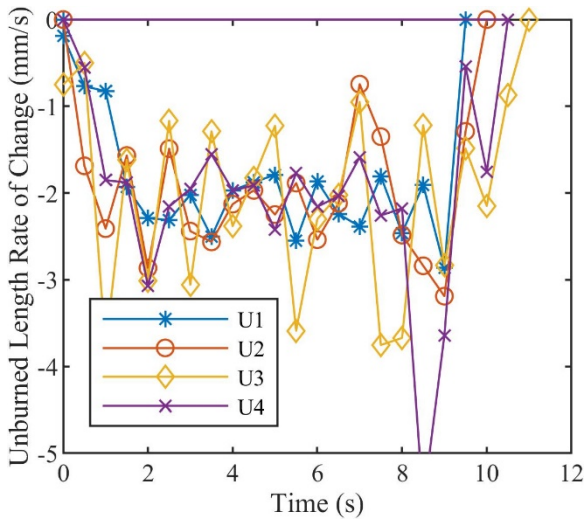

a

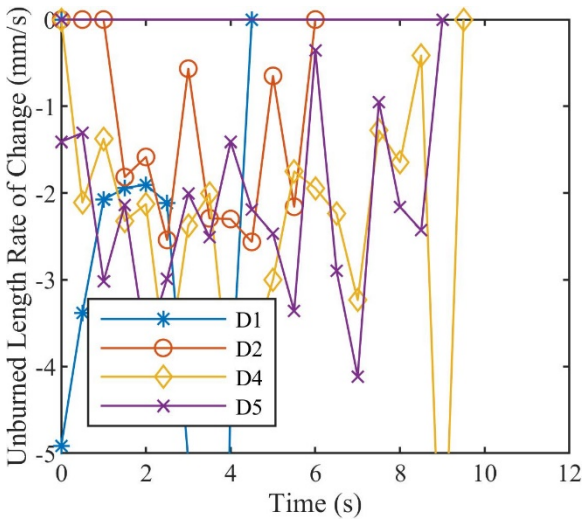

b

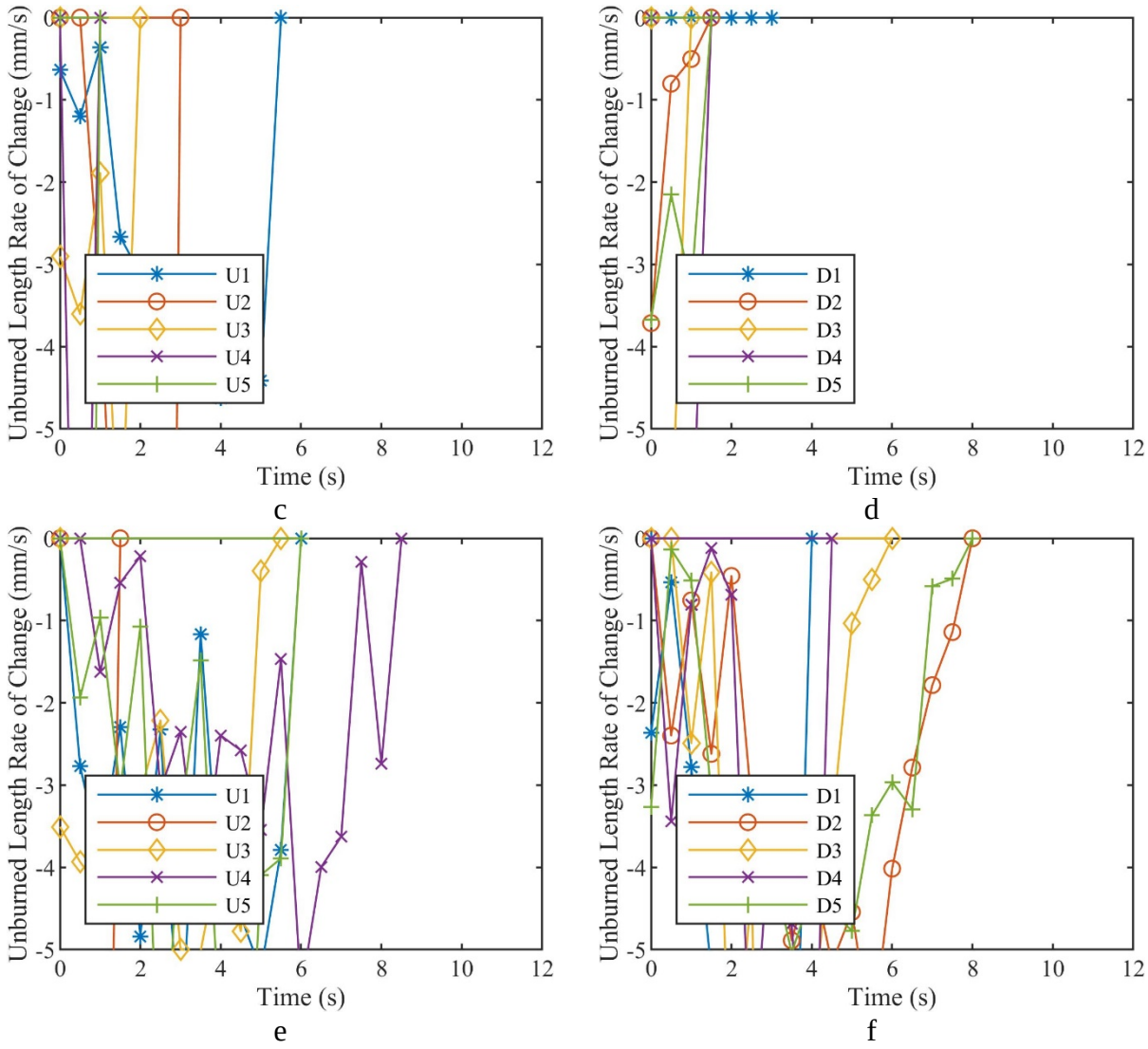

Fig. 23: Burning Rate vs. Time for Propellants with Aluminum

Fig. 24 shows the burning rate versus time for propellants without aluminum with an interval of calculation of at every half second. The burn rate of undegraded propellant 4, shown in Fig. 24(a), had a standard deviation of 1.16 mm/s and an average burn rate of -0.97 mm/s. The burn rate of degraded propellant 4, shown in Fig. 24(b), had a standard deviation of 1.56 mm/s and an average burn rate of -1.58 mm/s. The burn rate of undegraded propellant 5, shown in Fig. 24(c), had a standard deviation of 1.06 mm/s and an average burn rate of -2.08 mm/s. The burn rate of degraded propellant 5, shown in Fig. 24(d), had a standard deviation of 1.88 mm/s and an average burn rate

of -1.95 mm/s. The burn rate of undegraded propellant 6, shown in Fig. 24(e), had a standard deviation of 1.84 mm/s and an average burn rate of -3.33 mm/s. The burn rate of degraded propellant 6, shown in Fig. 24(f), had a standard deviation of 1.80 mm/s and an average burn rate of -2.03 mm/s.

The average burn rates of each experiment are displayed in Fig. 24 shows the burning rate versus time for propellants without aluminum with an interval of calculation of at every half second. The burn rate of undegraded propellant 4, shown in Fig. 24(a), had a standard deviation of 1.16 mm/s and an average burn rate of -0.97 mm/s. The burn rate of degraded propellant 4, shown in Fig. 24(b), had a standard deviation of 1.56 mm/s and an average burn rate of -1.58 mm/s. The burn rate of undegraded propellant 5, shown in Fig. 24(c), had a standard deviation of 1.06 mm/s and an average burn rate of -2.08 mm/s. The burn rate of degraded propellant 5, shown in Fig. 24(d), had a standard deviation of 1.88 mm/s and an average burn rate of -1.95 mm/s. The burn rate of undegraded propellant 6, shown in Fig. 24(e), had a standard deviation of 1.84 mm/s and an average burn rate of -3.33 mm/s. The burn rate of degraded propellant 6, shown in Fig. 24(f), had a standard deviation of 1.80 mm/s and an average burn rate of -2.03 mm/s.

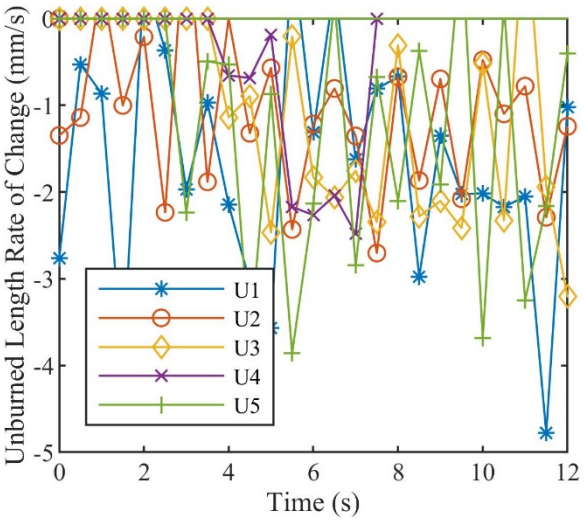
Unburned Length Rate of Change (mm/s)
Time (s)
U1
U2
U3
U4
U5

a

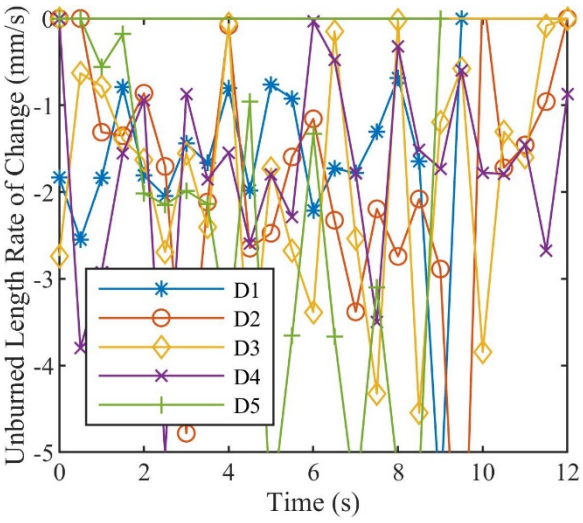
Unburned Length Rate of Change (mm/s)
Time (s)
D1
D2
D3
D4
D5

b

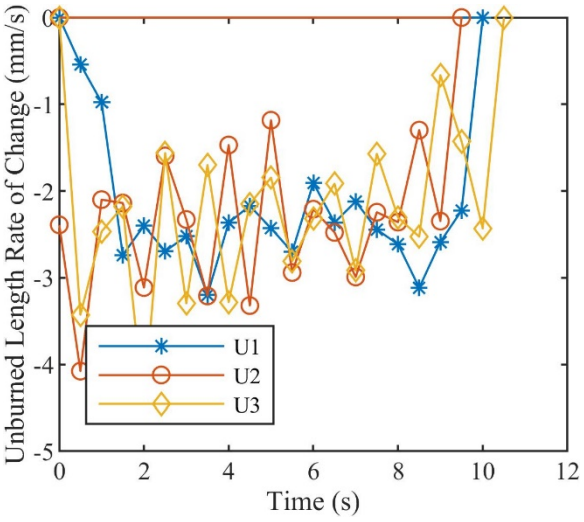
Unburned Length Rate of Change (mm/s)
Time (s)
U1
U2
U3

c

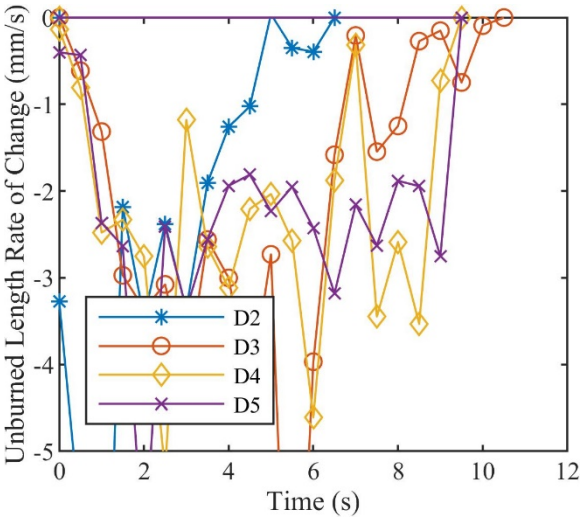
Unburned Length Rate of Change (mm/s)
Time (s)
D2
D3
D4
D5

d

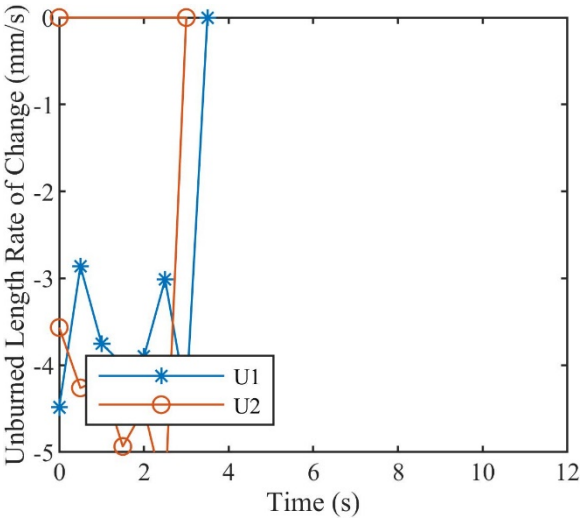
Unburned Length Rate of Change (mm/s)
Time (s)
U1
U2

e

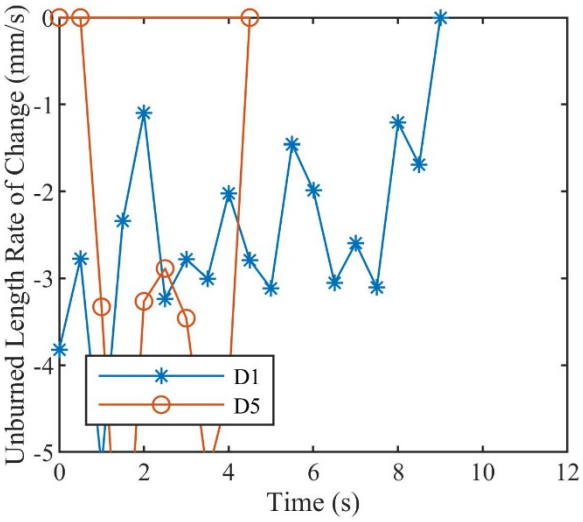
Unburned Length Rate of Change (mm/s)
Time (s)
D1
D5

f

Fig. 24: Burning Rate vs. Time for Propellants without Aluminum

The average burn rates of each experiment are displayed in Table 5. In Table 5, the x's denote samples which could not be processed using the MATLAB image processing. The burning rates of propellant 1 undegraded gathered with this technique were compared to the break-wire experiments and confirm that the measurements are within the expected range. Although the average burning rates may be different it is known that solid propellants burn faster at higher pressures, and since the break-wire experiment was run at atmospheric pressure and the strand burner experiments were run at 500 psi, the difference can be determined to be caused by the pressure difference.

Table 5: Average Burn Rates from Tested Propellants

Propellants	**1**	**2**	**3**	**4**	**5**	**6**
Un1	-1.59	-2.71	-2.33	-1.12	-2.01	-3.30
Un2	-1.73	-3.94	-1.96	-1.21	-2.08	-3.37
Un3	-1.98	x	-2.21	-1.21	-2.15	x
Un4	-1.86	x	-2.13	x	x	x
Un5	x	-2.72	-2.35	-1.03	x	x
Average 1	-1.79	-3.12	-2.19	-1.14	-2.08	-3.33
Deg1	-2.03	x	-2.37	-1.19	x	-2.49
Deg2	x	x	-2.78	-1.69	-2.14	x
Deg3	x	-2.27	-2.77	-1.65	-2.03	x
Deg4	-2.36	-6.75	-1.64	-1.68	-2.06	x
Deg5	-2.07	x	-2.78	-1.69	x	-1.57
Average 2	-2.16	-3.44	-2.47	-1.58	-2.04	-2.03
A2/ A1 multiplier	1.21	1.10	1.12	1.38	0.98	0.61

Propellants 1, 2, 3, and 4 followed the expected trend of the degraded samples on average burning at a faster rate, while propellant 6 followed a reverse of the expected trend. Propellant 6 had the least number of useable tests across all the propellant chemistries. Potentially with more samples,

the average across the tests could have led to an average that was an increase in the burning rate. Another possibility is that propellant 6 had the highest percentage of AP and the altered burn rate could have been dominated by a different effect of the degradation. Propellant 5 had very similar burning rates within 93% when comparing the data, but with propellant 5 degraded standard deviation being 179% of the undegraded truly differentiates the two degradations. Propellant 5 had several samples that were eliminated from the data set as they could not be analyzed due to particulate in the field of view and unnoticeable gaps between the propellant and the quartz sleeve. If all samples could have been analyzed, it is possible that the average would have been consistent with the hypothesis.

Qualitatively it can be speculated that the expansion of the degraded propellant samples decreased the density of the samples and contributed to the difference in the measure burning characteristics. Also, the darkening of the degraded samples could have increased the heat transferred to the samples and could have also contributed to the change in the burning characteristics. This is not expected to be the prime contributors to the change in burning characteristics, but it is worth the discussion and potential for follow-up experimentation.

This data indicates that the propellants with aluminum had a stronger reaction to the thermal degradation compared to the propellants without aluminum. This leads to the hypothesis that the added aluminum is the largest factor contributing to the propellant degradation in this thermal degradation scenario. It is speculated that the presence of aluminum contributes more to the degradation as it has a higher level of conductivity in comparison to the other propellant components. The aluminum better distributes the heat throughout the propellant.

Some issues encountered during the study included particulate obstructing the field of view, minor propellant geometry issues, and nitrogen flow rate control. In some tests, the particulate laden product gas, which was optically dense, was not carried out of the viewing area by the nitrogen co-flow. This led to smoke build-up within the observation area and obscured the image of the burning propellant. This could be alleviated in future investigations by increasing the co-flow velocity. During the experiments the flowrates were manually set with a flow controller and deviated approximately 1 cubic foot per minute. For higher repeatability of the flowrate, it is suggested to use a flow controller versus the flow meter used for this data set. Using a flow controller would allow a set mass flow to be kept throughout an entire test and could be reliably set for every test. Finally, in some of the tests, the propellant sample had an unnoticeable gap between the propellant and the inhibitor sleeve, thus causing an unusable burn pattern with the data analysis algorithm. The samples that were noticed to have a gap between the propellant and inhibitor sleeve during analysis were removed from the data sets.

Chapter 6. Conclusions

A high-pressure strand burner was developed for solid propellant experimentation. It was designed so that all components have a FOS higher than 3. The rig was hydrostatically tested to ensure that all fabricated components were safe. The propellant samples were mixed, cured, and thermally degraded in-house in order to ensure that the propellant components were mixed thoroughly and that no voids existed in the propellant samples. The propellant samples were cured at 333 K for 2 hours, and they were thermally degraded at 538 K for 5 minutes. The thermal degradation scenario was intended to simulate a fire near a weapons storage facility and the fire being quickly extinguished. Once the rig was ready for use, a series of experiments was run to develop an understanding of the effect of a high temperature, short duration thermal degradation on solid rocket propellants.

Propellants of various compositions of ammonium perchlorate, hydroxyl-terminated polybutadiene, and aluminum powder were mixed, cast, and cured. Propellants were thermally aged in an Across International laboratory oven to achieve an equivalent exposure time of 5 minutes at 538 degrees K, to simulate a weapons storage facility having a fire nearby and being quickly extinguished. Break wire tests were conducted in an atmospheric strand burner to validate the optical burn rate measurement technique used in the high-pressure strand burner. The break wire test burning rate was of good comparison to the burning rate of propellants throughout the literature survey. Having validated the optical method, tests were conducted in the high-pressure strand burner. It was hypothesized that the high temperature thermally degraded propellant samples would exhibit increased burning rates as compared to propellant samples that were not thermally degraded.

The propellants 1, 2, 3, and 4 confirmed the hypothesis of a higher burn rate of the thermally degraded propellant as compared to the undegraded propellant. Propellants 5 and 6 without aluminum had lower or equal observed burning rates of the degraded samples as compared to the undegraded samples. It is suspected that this is due to the number of samples that could be analyzed for these propellant formulations. Based on the findings of this study, it seems that aluminized propellants consistently burned faster than non-aluminized. Further, they exhibit significant sample-to-sample burn rate variation and time variation in burning rate. The question remains as to the exact cause of these observations. We hypothesize the added aluminum could be the largest factor causing change in the thermally degraded propellants. We speculate this is due to the thermal conductivity of aluminum because the aluminum better distributes the heat throughout the propellant, thus causing more degradation throughout the sample. These findings warrant investigation in a future study of this question with the objective of isolating the reacting factors for the propellants and codifying the factors of the propellant's burning efficiency. Understanding the reacting factors of the propellants would result in identifying the best component combinations for propellants stored over a long duration of time.

In summary, our findings indicate that there is an increase in the burning rate of propellants exposed to extreme high temperature. Also, that propellants containing aluminum will have more reaction to this thermal degradation scenario.

Chapter 7. Bibliography

[1] Bunyan, P., Cunliffe, A. V, Davist, A., and Kirby, F. A. *The Degradation and Stabilisation of Solid Rocket Propellants**. 1993.

[2] Ide, K. M., Ho, S., and Williams, D. R. G. “Fracture Behaviour of Accelerated Aged Solid Rocket Propellants.” *Journal of Materials Science*, Vol. 34, No. 17, 1999, pp. 4209–4218. https://doi.org/10.1023/A:1004690416667.

[3] Kadiresh, P. N., and Sridhar, B. T. N. “Experimental Study on Ballistic Behaviour of an Aluminised AP/HTPB Propellant during Accelerated Aging.” *Journal of Thermal Analysis and Calorimetry*, Vol. 100, No. 1, 2010, pp. 331–335. https://doi.org/10.1007/s10973-009-0569-3.

[4] Thomas, J. C., Sammet, T. E., Dillier, C. A. M., Demko, A. R., Rodriguez, F. A., and Petersen, E. L. “Aging Effects on the Burning Rates of Composite Solid Propellants with Nano-Additives.” 2018. https://doi.org/10.2514/1.B37189.

[5] McDonald, B. A., Rice, J. R., and Kirkham, M. W. “Humidity Induced Burning Rate Degradation of an Iron Oxide Catalyzed Ammonium Perchlorate/HTPB Composite Propellant.” 2014. https://doi.org/10.1016/j.combustflame.2013.08.014.

[6] Fleeman, E. L. Technologies for Future Precision Strike Missile Systems - Missile/Aircraft Integration. https://apps.dtic.mil/docs/citations/ADP010957. Accessed Apr. 30, 2019.

[7] Umholtz, P. D. “The History of Solid Rocket Propulsion and Aerojet.”

https://doi.org/10.2514/6.1999-2927.

[8] Fuente, J. L. de la, and Rodríguez, O. “Dynamic Mechanical Study on the Thermal Aging of a Hydroxyl-Terminated Polybutadiene-Based Energetic Composite.” *Journal of Applied Polymer Science*, Vol. 87, No. 14, 2003, pp. 2397–2405. https://doi.org/10.1002/app.12125.

[9] Kopp, C. *30-DefenceToday Military Technology Mil Tech Evolution of Guided Torpedoes*.

[10] Parr, T., and Hanson-Parr, D. “Optical Diagnostics of Solid-Propellant Flame Structures.” *Solid Propellant Chemistry, Combustion, and Motor Interior Ballistics*, Vol. 185, 2000, pp. 381–411. https://doi.org/10.2514/5.9781600866562.0381.0411.

[11] Eisenreich, N., Kugler, H. P., and Sinn, F. “An Optical System for Measuring the Burning Rate of Solid Propellant Strands.” *Propellants, Explosives, Pyrotechnics*, Vol. 12, No. 3, 1987, pp. 78–80. https://doi.org/10.1002/prep.19870120304.

[12] Fry, R. S. (JHU/CPIA). Evaluation of Methods for Solid Propellant Burn Rate Measurement. 0704. Volume 298.

[13] Yaman, H., Çelik, V., and Deg ˘irmenci, E. “Experimental Investigation of the Factors Affecting the Burning Rate of Solid Rocket Propellants.” 2014. https://doi.org/10.1016/j.fuel.2013.05.033.

[14] Powell, M. S., Gunduz, I. W., Shang, W., Chen, J., Son, S. F., Chen, Y., and Guildenbecher, D. R. “Agglomerate Sizing in Aluminized Propellants Using Digital Inline

Holography and Traditional Diagnostics.” 2018. https://doi.org/10.2514/1.B36859.

[15] Pressure Determination | Quartz Discs & Plates | Momentive. https://www.momentive.com/en-us/categories/quartz/pressure-determination. Accessed Aug. 3, 2020.

[16] Perry, E. H. Investigations of the T-Burner and Its Role in Combustion Instability Studies. *California Institute of Technology*.

[17] Ramsey, F. L., and Schafer, D. W. *The Statistical Sleuth: A Course in Methods of Data Analysis*. Cengage Learning, 2020.

[18] Humble, R. W., Henry, G. N., and Larson, W. J. *Space Propulsion Analysis and Design*. McGraw Hill.

[19] Culick, F. E. C. (California I. of T. T-Burner Testing of Metallized Solid Propellants. October.